Curvature effect-based modeling and experimentation of the material removal in polishing optical surfaces using a flexible ball-end tool

Chenchun Shi,[1,2] **Chunjin Wang,**[1,4] (iD) **Chi Fai Cheung,**[1,5] (iD)
Zili Zhang,[1] **Ze Li,**[1] **Lai Ting Ho,**[1] **Weijie Deng,**[3]
and Xuejun Zhang[2]

[1] *State Key Laboratory of Ultra-precision Machining Technology, Department of Industrial and Systems Engineering, The Hong Kong Polytechnic University, Hung Hom, Kowloon, Hong Kong, China*
[2] *Faculty of Mechanical Engineering and Mechanics, Ningbo University, Ningbo, 315211, China*
[3] *Changchun Institute of Optics, Fine Mechanics and Physics, Chinese Academy of Sciences, Changchun, 130033, China*
[4] *chunjin.wang@polyu.edu.hk*
[5] *benny.cheung@polyu.edu.hk*

Abstract: Optical surfaces with high quality have been widely applied in high-tech industries for their excellent performances. To precision manufacture those surfaces efficiently and effectively, various machining technologies involved become extremely crucial. As one of the promising ultra-precision machining technologies, inflated or solid elastic tool polishing has attracted more attention for its own superiority. However, there is still lack of understanding on material removal mechanisms especially with the consideration of curvature effect, and it is of great importance to determine the surface quality and form control in ultra-precision polishing process. In this paper, originating from the famous macro-scale Preston equation, the curvature effect-based material removal model in polishing using a flexible ball-end tool has been developed successfully on the basis of two key sub-models, one is the generic model of effective relative velocity and the other refers to the semi-experimental contact pressure model. A series of spot polishing experiments subsequently are conducted on concave surfaces with a curvature radius range from 75 mm to 225 mm. The experimentally measured section profiles of polishing spots do match well with the predicted data, which verifies the effectiveness of the proposed material removal model. On the measured polishing spots, it is also observed that there have two nonuniform material removal phenomena, one is analyzed along the central axis and the other is discussed by two regions symmetrical about the central axis. Compared with the effective relative velocity, it is found that, the contact pressure is more sensitive to curvature effect by investigating the variation of maximum removal depth within a broader curvature radius range from 75 mm to 1000 mm. This study can provide a valuable foundation for polishing optical surfaces with deterministic removal.

1. Introduction

Optical surfaces with high form accuracy and excellent surface finish are extensively employed in advanced optical industries for the superiorities including simplification of system structure, increase of optical functionality, improvement of optical performance, etc [1–3]. Besides the precision optical applications, freeform metallic surfaces also have been used widely for example in the field of mould [4,5]. In order to fabricate those required freeform surfaces efficiently and effectively, various machining technologies involved become extremely crucial. Generally, after the final shape defining processes such as grinding, ultra-precision polishing as the last step in the whole process chain is of fundamental importance and plays a key role in removing the residual

surface topography, improving the surface roughness, and thereby achieving a desired surface with high quality [6]. As a result, quite a few computer-controlled polishing technologies have emerged which are not just limited to ion beam finishing [7], fluid jet polishing [8,9], stressed lap polishing [10], magnetorheological jet polishing [11]. Among them, computer-controlled bonnet polishing is commonly regarded as one of the promising technologies to fabricate optical freeform components due to its advantages of high material removal rate, compliant contact in sub-aperture region, good adaptability to complex surface, flexibly controllable spot size, and acceptable cost performance, etc [12–18]. Also, the adopted polishing tool in the concept of bonnet polishing process could be either inflated or solid elastic [18].

It then is well-known that a precise and stable tool influence function model to predict the material removal during bonnet polishing is of paramount significance, since the surface generation in the polishing process is related to the convolution of tool influence function and dwell time [16,19]. Moreover, a reliable tool influence function model is also beneficial to avoid the process generation and measurement of an experimental tool influence function so that the production cycle can be properly shortened [20]. Indeed, there have been some previous research work concerning the material removal model of bonnet polishing. The material removal in inflated or solid elastic tool polishing is usually characterized by the classical Preston equation which is seen as macro-model and expressed as [20–24]

$$MRD = K\sigma Vt \tag{1}$$

where *MRD* denotes the material removal depth in certain time t, while K is the Preston coefficient associated with abrasive size, slurry concentration, polishing pad, workpiece material, etc. σ and V represent the applied working pressure and relative velocity distribution on the contact area, respectively. Since K is generally considered to be invariant during the polishing process, the modeling of material removal actually depends on the calculation of σ and V. Nonetheless, other versions of Preston model also have been reported on the basis of Eq. (1). Pan *et al.* [25] took the interfacial friction coefficient μ between inflated polishing tool and flat workpiece into account and Eq. (1) was modified as $MRD = K\mu\sigma Vt$. Suratwala *et al.* [3] proposed that $MRD = K\mu\sigma Vt + K_{ps}\tau Vt$ to examine the material removal of flat workpiece using a hemispherical pad-foam polishing tool, where K_{ps} denotes the shear-based Preston constant and τ is the shear stress. Some modified expressions also include $MRD = K\sigma^{2/3}Vt$ [26] and $MRD = K(\sigma V)^{1/2}t$ [27] but they were effectively applied in chemical-mechanical polishing rather than flexible bonnet polishing. Afterwards, in terms of micro-modeling, Cao *et al.* developed the multi-scale material removal model via the detailed expansion of K shown in Eq. (1) for bonnet polishing on flat workpiece [16,28]. Shi *et al.* [17] established the micro-analysis model for studying material removal mechanisms of bonnet polishing on the sample with flat surface, where the material removal was assumed to be primarily attributed to the abrasive wear by the abrasive particles in slurry, as well as the wear effect from polishing pad asperities. Furthermore, the improved micro-analysis model was published by incorporating the pad wear effect with cumulative polishing time [29]. No matter macro-model or micro-model, both of them could be acknowledged as one of the effective approaches to scientifically explain the material removal in polishing.

However, these aforementioned material removal models in bonnet polishing focused on flat workpiece more, in other words, the local curvature effect is supposed to be put into consideration thoroughly for polishing freeform surfaces. Hence, the curvature effect-based modeling of material removal deserves to be researched deeply and urgently. Song *et al.* investigated the material removal of bonnet polishing both theoretically and experimentally but on the convex workpieces only, and the curvature radius range was relatively narrow [30–32]. Zhong *et al.* [19] developed the time-varying tool influence function model of bonnet polishing for aspheric surfaces, but it was experimentally verified with a limited data set (convex radius of 500 mm,

flat surface, concave radius of 500 mm, totally three), and the undesired large deviation of peak removal rate between experimental and simulated results occurred as well. Suratwala *et al.* [33] studied the effect of workpiece curvature on the tool influence function during hemispherical sub-aperture tool glass polishing, whereas only one curvature radius of 500 mm was researched on the aspect of concave surface. By using a spherical tool, Yang and Lee [34] took the small aspherical lens die as the polished sample and disclosed the local material removal mechanism considering curvature effect, where the analyzed curved surfaces all were concave, but the radii were chosen from 10 mm to 50 mm with an interval of 10 mm, so the evaluated range of curvature radius still was thought to be not broad enough. As a result, little attention has been paid to the curvature effect of concave surfaces featured with broad radius range and small radius interval.

On the modelling methods, σ and V were commonly considered as the two key parameters and followed with interest. The interfacial contact pressure between an inflated or solid elastic tool and the workpiece with curved surface usually could be calculated by means of finite element analysis [19], Hertz contact theory [30–32,34], Hertzian contact mechanics based elastic sphere-sphere contact mechanics model [33], even experimental measurement with a static pressure sensor [19], etc. Nevertheless, the measurement accuracy of pressure sensor compressed on various curved surfaces, instead of flat surface, may be affected more or less. Hence, the theoretical models of contact pressure become more acceptable to facilitate the final establishment of material removal model. Owing to the complexity of interfacial contact pressure in the actual polishing environment, it is still a problem needed to be addressed urgently for how to properly determine the interfacial contact pressure with high prediction accuracy. As for the derivation of relative velocity with curvature effect, it had been well recognized based on the kinematic theory. Note that, it is only the tangential component of relative velocity on the local polishing area that affects the material removal [34]. Nevertheless, the linear velocity, but not the tangential component, was directly assumed as the relative velocity indicated in some research work [4,19,30–32]. Also, the detailed derivation of relative velocity with curvature effect could not be found in the work by Suratwala *et al.* [33]. In addition, more attentions have been poured into tilted polishing mode, so the generic model of relative velocity with curvature effect under continuous precession mode has not been developed yet. Although Yang *et al.* proposed the generic model of relative velocity, the offset as one of the vital polishing process parameters was neglected simply [34]. Hence, the effective relative velocity with curvature effect still has to be modified completely.

In our study, a generic model of effective relative velocity with curvature effect is established by posture description on the basis of kinematic theory and an alternative method to calculate contact pressure with semi-experimental feature also is interestingly proposed aiming to obtain the interfacial contact pressure as accurate as possible, which facilitates the ultimate development of curvature effect-based material removal model in polishing using a flexible ball-end tool. Subsequently, a series of concave surfaces with broad radius range and small radius interval are taken as the investigated curved workpieces to sufficiently verify the correctness and effectiveness of the proposed material removal model. Moreover, some experimental phenomena on polishing spots are well presented and carefully analyzed so as to reveal the material removal mechanisms, such as the interpretations of nonuniform material removal, and which one is affected by curvature effect more significantly between the two key parameters σ and V, as well as how is the variation trend of maximum removal depth of polishing spot with the changing curvature radius, etc. It is expected and also believed that this research can provide some good insights and valuable reference to the peer researchers for instance in the field of ultra-precision polishing technologies.

2. Theoretical modeling and analysis

In this paper, the theoretical modeling of material removal in polishing using a flexible ball-end tool is thoroughly conducted by incorporating the workpiece curvature effect. The modeling method originates from the well-known Preston equation illustrated in Eq. (1). As a result, as two

key parameters, both the modification of relative velocity and the calculation of contact pressure distribution are carried out and given clearly.

2.1.   Modeling of the effective relative velocity

2.1.1.   Relative velocity for flat surface

Based on the kinematic theory, the velocity of the flexible ball-end polishing tool relative to the workpiece on the contact area can be available. To distinguish the discrepancy between the relative velocities with and without the consideration of curvature effect, the flat workpiece is taken as the analyzed object first, then the curved workpiece.

As shown in Fig. 1, the flat workpiece is compressed by an ideal flexible ball-end tool with the radius of R_b, and the offset is d, so the circular contact area with the radius of a occurs, its center is signed as the point O_w. The space rectangular coordinate system $\{A\}$ is established, and the origin O_A is fixed at the center of the ball-end polishing tool. There are two rotational axes marked as L axis and Z_A axis, which correspond to the two angular velocities ω_1 and ω_2, respectively. The angle between L axis and Z_A axis is named as inclination angle ϕ. It can be observed from Fig. 1(b) that, the plane MQN coincides with the plane $O_AY_AZ_A$. Point P is located on the contact area, and its coordinates are (x_P, y_P, z_P) in the reference coordinate system $\{A\}$. The point O_r on L axis (MN axis) is the swing center of point P. Besides, the symbols α and θ refer to the angle between O_wZ_A axis and O_AP axis as well as the angle between O_wP and O_wN, respectively. The detailed mathematical expression is employed to describe the kinematic relationship as shown in Fig. 1.
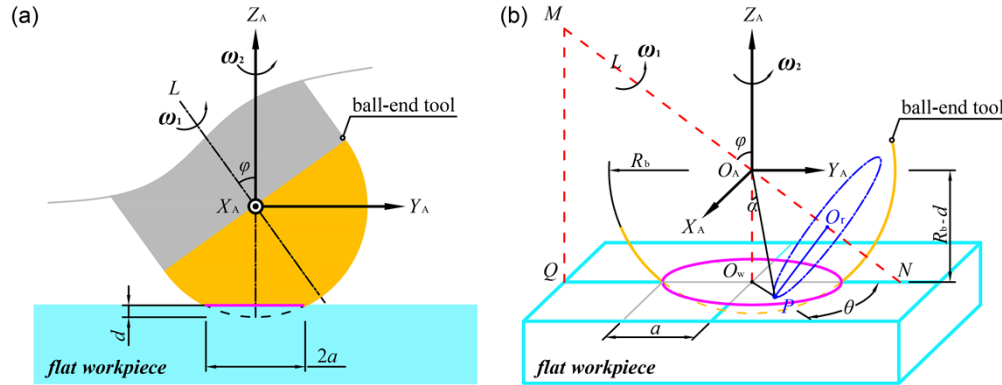
Fig. 1. Graphical illustration of the contact between the flat workpiece and a flexible ball-end polishing tool. (a) Two dimensional view along the negative direction of X_A axis, and (b) three dimensional view.

Due to the unit of ω_1 is set as rad/s, its expression can be given as follows:

$$\omega_1 = \frac{2\pi \cdot n_1}{60}(0, \ -\sin\phi, \ \cos\phi) \qquad (2)$$

where n_1 denotes tool rotational speed of L axis with the unit of rpm. Afterwards, the point $P(x_P, y_P, z_P)$ can be known as

$$\begin{pmatrix} x_P \\ y_P \\ z_P \end{pmatrix} = \begin{pmatrix} O_wP \cdot \sin\theta \\ O_wP \cdot \cos\theta \\ -(R_b - d) \end{pmatrix} = \begin{pmatrix} O_AO_w \cdot \tan\alpha \cdot \sin\theta \\ O_AO_w \cdot \tan\alpha \cdot \cos\theta \\ -(R_b - d) \end{pmatrix} = \begin{pmatrix} (R_b - d) \cdot \tan\alpha \cdot \sin\theta \\ (R_b - d) \cdot \tan\alpha \cdot \cos\theta \\ -(R_b - d) \end{pmatrix} \qquad (3)$$

where $\theta \in [0, 2\pi]$ and $\alpha \in [0, \arctan(a/(R_b - d))]$. If the coordinates of point O_r are defined as $(0, y_r, -y_r \cot \phi)$, the vectors $\boldsymbol{O_A O_r}$ and $\boldsymbol{O_r P}$ are then obtained as

$$\boldsymbol{O_A O_r} = (0, \ y_r, \ -y_r \cot \phi) \tag{4}$$

$$\boldsymbol{O_r P} = \boldsymbol{O_A P} - \boldsymbol{O_A O_r} = (x_U, y_V, z_w) = \begin{pmatrix} (R_b - d) \tan \alpha \sin \theta \\ (R_b - d) \tan \alpha \cos \theta - y_r \\ -(R_b - d) + y_r \cot \phi \end{pmatrix} \tag{5}$$

Because of $\boldsymbol{O_A O_r} \perp \boldsymbol{O_r P}$, there has $\boldsymbol{O_A O_r} \cdot \boldsymbol{O_r P} = 0$, and it is determined specifically as

$$0 \cdot x_U + y_r \cdot y_V + (-y_r \cot \phi) \cdot z_w = 0$$
$$\Rightarrow 0 \cdot ((R_b - d) \tan \alpha \sin \theta) + y_r \cdot ((R_b - d) \tan \alpha \cos \theta - y_r) \tag{6}$$
$$+ (-y_r \cot \phi) \cdot (-(R_b - d) + y_r \cot \phi) = 0$$

From Eq. (6), the value of y_r can be solved ultimately as

$$y_r = \frac{(R_b - d)(\tan \alpha \cos \theta + \cot \phi)}{1 + (\cot \phi)^2} \tag{7}$$

Substituting Eq. (7) into Eq. (4) and Eq. (5), both of $\boldsymbol{O_A O_r}$ and $\boldsymbol{O_r P}$ are determined. Hence, the relative velocity $\boldsymbol{V_{P1}}$ induced only by the rotation of L axis that can be given as follows:

$$\boldsymbol{V_{P1}} = \boldsymbol{\omega_1} \times \boldsymbol{O_r P} = \begin{vmatrix} \boldsymbol{i} & \boldsymbol{j} & \boldsymbol{k} \\ 0 & -\frac{\pi \cdot n_1 \sin \phi}{30} & \frac{\pi \cdot n_1 \cos \phi}{30} \\ x_U & y_V & z_w \end{vmatrix}$$
$$= \frac{\pi \cdot n_1}{30} [(-z_w \sin \phi - y_V \cos \phi) \cdot \boldsymbol{i} + x_U \cos \phi \cdot \boldsymbol{j} + x_U \sin \phi \cdot \boldsymbol{k}] \tag{8}$$

where the mathematical expressions of x_U, y_V and z_w can be found in Eq. (5). Analogously, the relative velocity $\boldsymbol{V_{P2}}$ induced by the rotation of Z_A axis could be obtained, it should be

$$\boldsymbol{V_{P2}} = \boldsymbol{\omega_2} \times \boldsymbol{O_w P} = \begin{vmatrix} \boldsymbol{i} & \boldsymbol{j} & \boldsymbol{k} \\ 0 & 0 & \pi \cdot n_2 / 30 \\ (R_b - d) \tan \alpha \sin \theta & (R_b - d) \tan \alpha \cos \theta & 0 \end{vmatrix}$$
$$= -\frac{\pi \cdot n_2}{30} (R_b - d) \tan \alpha \cos \theta \cdot \boldsymbol{i} + \frac{\pi \cdot n_2}{30} (R_b - d) \tan \alpha \sin \theta \cdot \boldsymbol{j} + 0 \cdot \boldsymbol{k} \tag{9}$$

where n_2 denotes tool rotational speed of Z_A axis with the unit of rpm. Accordingly, the relative velocity $\boldsymbol{V_P}$ induced by the rotation of L axis together with that of Z_A axis can be determined as follows:

$$\boldsymbol{V_P} = \boldsymbol{V_{P1}} + \boldsymbol{V_{P2}} = \begin{pmatrix} V_{Px} \\ V_{Py} \\ V_{Pz} \end{pmatrix}$$
$$= \begin{pmatrix} (\pi \cdot n_1 / 30)(-z_w \sin \phi - y_V \cos \phi) - (\pi \cdot n_2 / 30)(R_b - d) \tan \alpha \cos \theta \\ (\pi \cdot n_1 / 30) x_U \cos \phi + (\pi \cdot n_2 / 30)(R_b - d) \tan \alpha \sin \theta \\ (\pi \cdot n_1 / 30) x_U \sin \phi \end{pmatrix} \tag{10}$$

As shown in Fig. 1, what must be well pointed out is that, the effective relative velocity playing a role in material removal within the contact area is V_{P_eff}, its mathematical expression can be written as

$$|\boldsymbol{V_{P\_eff}}| = V_{P\_eff} = \sqrt{V_{Px}^2 + V_{Py}^2} \qquad (11)$$

In other words, $\boldsymbol{V_{P\_eff}}$ refers to the projection of vector $\boldsymbol{V_P}$ into the plane $X_A O_A Y_A$. Where V_{Px} and V_{Py} are supposed to be captured from Eq. (10). Also, it is found from Eq. (11) that the component V_{Pz} is useless for polishing flat workpiece.

2.1.2.   Relative velocity with the consideration of curvature effect

According to Eq. (2) to Eq. (11), under continuous precession mode (i.e., $n_1 \neq 0$ and $n_2 \neq 0$), the detailed calculation of relative velocity without the consideration of curvature effect has already been available. Furthermore, the emphasis in this paper is placed on the relative velocity incorporating curvature effect. On the basis of aforementioned modeling of relative velocity for polishing flat surface, the workpiece featured with concave surface is adopted as the analyzed example.

As shown in Fig. 2, the three dimensional (3D) contact area can be formed when the workpiece moves towards to the ball-end tool along the positive direction of Z_A axis with a displacement of d. The assumption proposed here is that the flexible ball-end polishing tool with solid elastic property completely fits the rigid workpiece, so the 3D contact area has the same curvature with that of the concave workpiece, and the corresponding radius is marked as R_w in Fig. 2(c). Besides the existing $\{A\}$ fixed on the ball-end tool, the space rectangular coordinate system $\{w1\}$ is also established, and the origin O_{w1} is fixed just at the center of the concave workpiece. The only difference between $\{A\}$ and $\{w1\}$ lies in the distance along $O_A Z_A$ axis, so that $O_{w1} O_A$ representing this distance can be determined and known as $R_w - (R_b - d)$. Moreover, the imaging that the three dimensional contact area is cut to many planes which all are parallel to plane $X_A O_A Y_A$ and numbered in sequence, any point on the three dimensional contact area is effectively located on the circular boundary of plane i ($i \to \infty$).
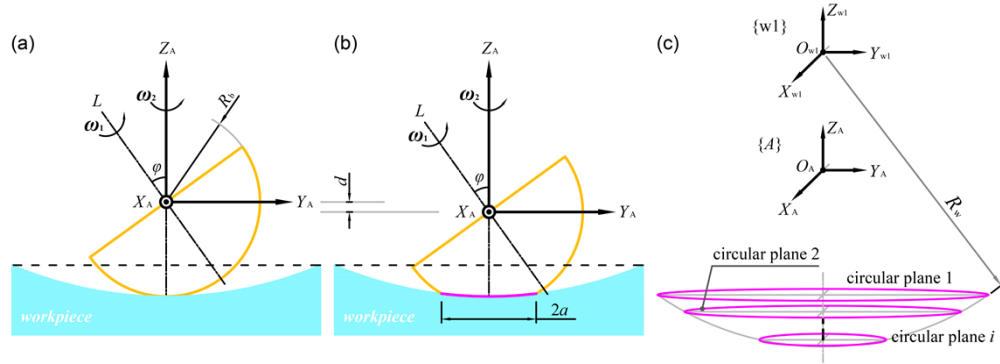
Fig. 2. Schematic diagram of the contact between the concave workpiece and a flexible ball-end polishing tool (a) without compression, (b) with the offset of d, and (c) three dimensional contact area.

What can be seen from Fig. 3(a) is that, P_{ij} is the point located on the three dimensional contact area. Also, it becomes accessible to understand that P_{ij} is the point on the circular boundary of plane i as well, where j ($j \to \infty$) denotes the number of those points on the ith circular boundary, as depicted in Fig. 3(b). In addition, P_w signifies the point on the bottom of this three dimensional contact area. P_{ij}' means the projection of P_{ij} into plane 1. d_0 refers to the perpendicular gap between P_w and plane 1, which can be considered as the maximum depth of

the three dimensional contact area. Lastly, β represents the angle between tangent plane ij and horizontal plane $X_A O_A Y_A$ as well as that between $O_{w1} P_{ij}$ and $O_A O_{w1}$. The relationships among various points on the three dimensional contact area are supposed to be exemplified. For the points P_{11}, P_{41} and P_{61} in Fig. 3(a), they are all located in the plane $O_A Y_A Z_A$ and have the same θ, but the different β. For another four points P_{i1}, P_{i2}, P_{i3} and P_{i4} presented in Fig. 3(b), they are all located in the same horizontal plane and have the same β, but the different θ.

Still taking $\{A\}$ as the reference coordinate system, the coordinates of point P_{ij} can be written as $(^A x_P, \, ^A y_P, \, ^A z_P)$, and they are determined specifically as follows

$$
\begin{pmatrix} ^A x_P \\ ^A y_P \\ ^A z_P \end{pmatrix} = \begin{pmatrix} ^{w1} x_P \\ ^{w1} y_P \\ -|^{w1} z_P| + O_{w1} O_A \end{pmatrix} = \begin{pmatrix} (R_b - d - d_0)\tan\alpha \sin\theta \\ (R_b - d - d_0)\tan\alpha \cos\theta \\ -\sqrt{R_w^2 - (^{w1} x_P)^2 - (^{w1} y_P)^2} + (R_w - (R_b - d)) \end{pmatrix} \tag{12}
$$

where $^{w1} z_P$ signifies the Z coordinate of point P_{ij} in $\{w1\}$. There also have $^A x_P = {}^{w1} x_P$ and $^A y_P = {}^{w1} y_P$, and d_0 is obtained as

$$
d_0 = R_w - \sqrt{R_w^2 - a^2} \tag{13}
$$

Afterwards, the relative velocities $^A V_{P1\_C}$ and $^A V_{P2\_C}$ purely produced by the rotations of L axis and Z_A axis are determined, respectively. They can be expressed as

$$
\begin{aligned}
^A V_{P1\_C} &= \omega_1 \times O_A P \\
&= \frac{n_1 \pi}{30} \begin{pmatrix} -{}^A y_P \cos\phi - \left(d - R_b + R_w - \sqrt{R_w^2 - {}^A y_P^2 - {}^A x_P^2}\right)\sin\phi \\ {}^A x_P \cos\phi \\ {}^A x_P \sin\phi \end{pmatrix}
\end{aligned} \tag{14}
$$

$$
^A V_{P2\_C} = \omega_2 \times O_A P = \begin{pmatrix} -\frac{n_2 \pi}{30}{}^A y_P & \frac{n_2 \pi}{30}{}^A x_P & 0 \end{pmatrix}^T \tag{15}
$$

Consequently, the relative velocity $^A V_{P\_C}$ induced by the rotation of L axis together with that of Z_A axis can be obtained as follows:

$$
\begin{aligned}
^A V_{P\_C} &= {}^A V_{P1\_C} + {}^A V_{P2\_C} \\
&= \begin{pmatrix} \frac{n_1 \pi}{30}\left(-{}^A y_P \cos\phi - \left(d - R_b + R_w - \sqrt{R_w^2 - {}^A y_P^2 - {}^A x_P^2}\right)\sin\phi\right) - \frac{n_2 \pi}{30}{}^A y_P \\ \frac{n_1 \pi}{30}{}^A x_P \cos\phi + \frac{n_2 \pi}{30}{}^A x_P \\ \frac{n_1 \pi}{30}{}^A x_P \sin\phi \end{pmatrix}
\end{aligned} \tag{16}
$$

where the subscript C as one marker means the curvature effect, and the superscript A as another marker represents that the three velocity vectors are determined based on the reference coordinate system $\{A\}$. Similar to Eq. (11), there also has an effective relative velocity contributing to material removal within the three dimensional contact area as shown in Fig. 3. The pose description in kinematic theory is employed here to solve the effective relative velocity. It is noted that the effective relative velocity seems not to be given further in the published work by [4,19,30–32].

As shown in Fig. 3(c), the other two space rectangular coordinate systems $\{w2\}$ and $\{B\}$ are set up. That $\{w2\}$ can be achieved through the rotation of $\{w1\}$ around $O_{w1} Z_{w1}$ axis with an angle of θ, while $\{B\}$ is attained by the rotation of $\{A\}$ around $O_A Z_A$ axis with an angle of θ
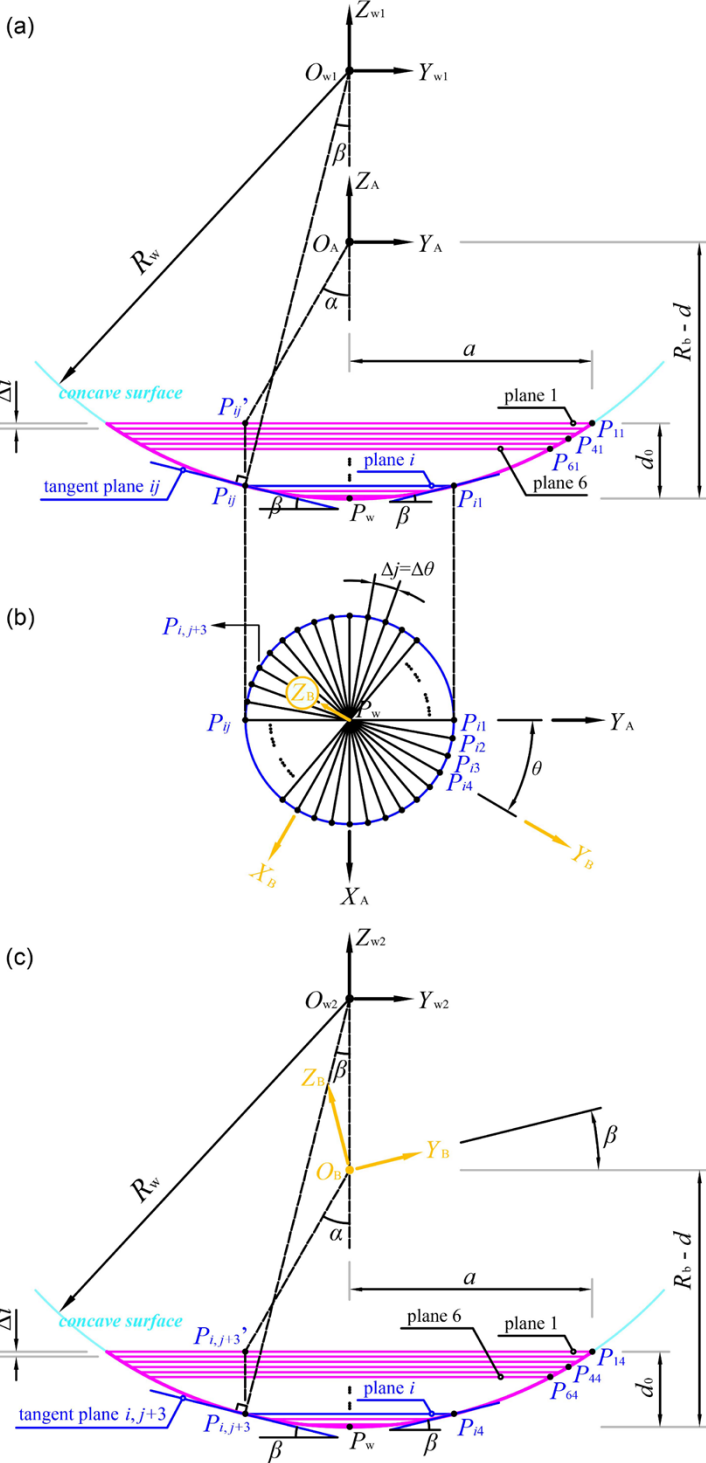
Fig. 3. Schematic diagram of solving the effective relative velocity with curvature effect (a) view along the negative direction of $O_A X_A$ axis, (b) the ith circular boundary within the three dimensional contact area, and (c) view along the negative direction of $O_{w2} X_{w2}$ axis.

first, then immediately is the rotational angle β around $O_A X_A$ axis. Hence, the rotation matrix denoting the orientation of $\{B\}$ relative to $\{A\}$ is given as

$$
{}^A_B R =
\begin{bmatrix}
\cos\theta & -\sin\theta & 0 \\
\sin\theta & \cos\theta & 0 \\
0 & 0 & 1
\end{bmatrix}
\cdot
\begin{bmatrix}
1 & 0 & 0 \\
0 & \cos\beta & -\sin\beta \\
0 & \sin\beta & \cos\beta
\end{bmatrix}
\tag{17}
$$

What is more, the relationship between ${}^A V_{\mathbf{P\_C}}$ and ${}^B V_{\mathbf{P\_C}}$ becomes explicit and is given as following

$$
{}^A V_{\mathbf{P\_C}} = {}^A_B R \cdot {}^B V_{\mathbf{P\_C}} \;\Rightarrow\; {}^B V_{\mathbf{P\_C}} = ({}^A_B R)^{-1} \cdot {}^A V_{\mathbf{P\_C}} =
\begin{pmatrix}
{}^B V_{\mathrm{P\_}Cx} \\
{}^B V_{\mathrm{P\_}Cy} \\
{}^B V_{\mathrm{P\_}Cz}
\end{pmatrix}
$$

$$
= \frac{\pi}{30}
\begin{pmatrix}
{}^A x_{\mathrm{P}}(n_2 + n_1 \cos\phi)\sin\theta - \cos\theta(n_2 {}^A y_{\mathrm{P}} + n_1 {}^A y_{\mathrm{P}} \cos\phi + n_1 {}^A z_{\mathrm{P}} \sin\phi) \\
n_1 {}^A x_{\mathrm{P}} \sin\beta \sin\phi + \cos\beta({}^A x_{\mathrm{P}} \cos\theta(n_2 + n_1 \cos\phi) + \sin\theta(n_2 {}^A y_{\mathrm{P}} + n_1 {}^A y_{\mathrm{P}} \cos\phi + n_1 {}^A z_{\mathrm{P}} \sin\phi)) \\
-{}^A x_{\mathrm{P}} \cos\theta(n_2 + n_1 \cos\phi)\sin\beta + n_1 {}^A x_{\mathrm{P}} \cos\beta \sin\phi - \sin\beta \sin\theta(n_2 {}^A y_{\mathrm{P}} + n_1 {}^A y_{\mathrm{P}} \cos\phi + n_1 {}^A z_{\mathrm{P}} \sin\phi)
\end{pmatrix}
$$
$$\tag{18}$$

where ${}^A z_{\mathrm{P}}$ can be found in Eq. (12), while θ and β are supposed to be

$$
\theta = -\arctan\left(\frac{{}^A x_{\mathrm{P}}}{{}^A y_{\mathrm{P}}}\right), \; {}^A y_{\mathrm{P}} > 0; \;\; \theta = -\arctan\left(\frac{{}^A x_{\mathrm{P}}}{{}^A y_{\mathrm{P}}}\right) + \pi, \; {}^A y_{\mathrm{P}} < 0
\tag{19}
$$

$$
\beta = \arccos \frac{\sqrt{R_{\mathrm{w}}^2 - ({}^{w1} x_{\mathrm{P}})^2 - ({}^{w1} y_{\mathrm{P}})^2}}{R_{\mathrm{w}}} = \arccos \frac{\sqrt{R_{\mathrm{w}}^2 - ({}^A x_{\mathrm{P}})^2 - ({}^A y_{\mathrm{P}})^2}}{R_{\mathrm{w}}}
$$
$$
= \arccos \frac{\sqrt{R_{\mathrm{w}}^2 - ((R_{\mathrm{b}} - d - d_0)\tan\alpha \sin\theta)^2 - ((R_{\mathrm{b}} - d - d_0)\tan\alpha \cos\theta)^2}}{R_{\mathrm{w}}}
\tag{20}
$$

Until now, the effective relative velocity leading to material removal within the three dimensional contact area can be identified as

$$
\left|{}^B V_{\mathbf{P\_C\_eff}}\right| = {}^B V_{\mathrm{P\_C\_eff}} = \sqrt{({}^B V_{\mathrm{P\_}Cx})^2 + ({}^B V_{\mathrm{P\_}Cy})^2}
\tag{21}
$$

where ${}^B V_{\mathbf{P\_C\_eff}}$ does signify the projection of vector ${}^B V_{\mathbf{P\_C}}$ into the plane $X_{\mathrm{b}} O_{\mathrm{b}} Y_{\mathrm{b}}$. Attention should be paid that, the tangent plane *ij* corresponding to point P_{ij} exhibited in Fig. 3(c) and the plane $X_{\mathrm{b}} O_{\mathrm{b}} Y_{\mathrm{b}}$ are parallel to each other. As for ${}^B V_{\mathrm{P\_}Cx}$ and ${}^B V_{\mathrm{P\_}Cy}$, they can be extracted in Eq. (18). Accordingly, the effective relative velocity resulting in material removal has been figured out clearly. The effective relative velocities determined in both Eq. (11) and Eq. (21) refer to the shear velocities parallel to the tangent plane *ij* of P_{ij}, and the tangent plane *ij* varies with the changing position of P_{ij} as shown in Fig. 3, so that the rotation matrix of Eq. (17) is introduced necessarily, nonetheless, there is only one same tangent plane *QNP* for polishing flat surface in Fig. 1, which significantly causes the radical difference between Eq. (11) and Eq. (21).

2.1.3. Contrastive analysis

No matter $V_{\mathrm{P\_eff}}$ shown in Eq. (11) for flat surface or ${}^B V_{\mathrm{P\_C\_eff}}$ that presented in Eq. (21) for concave surface, both of them are relevant tightly to the nonzero value of n_2. Hence, taking one arbitrary point P in the contact area as the researched sample, the effective relative velocity acting on this point P varies periodically with the polishing time t, which also means that $V_{\mathrm{P\_eff}}$

in Eq. (11) and $^{B}V_{P\_C\_eff}$ in Eq. (21) could be understood as the instantaneous relative velocities ($t = 0$) under continuous precession mode. According to Ref. [35], the parameter t is linked to θ_r, which can be expressed as follows:

$$\theta_r = \theta + \frac{360}{60}n_2 t \Rightarrow \theta_r = \theta + 6n_2 t \tag{22}$$

where θ_r is the relative position of this arbitrary point P to the ball-end tool. While θ denotes the initial relative position of this arbitrary point P to the ball-end tool in the contact area, and it also represents the angle between $O_w P$ and $O_w N$ shown in Fig. 1(b) and that between $O_A Y_A$ and $O_b Y_b$ depicted in Fig. 3(b). The units of t and θ_r in Eq. (22) are seconds and deg, respectively. If θ in Eqs. (11) and (21) is replaced by θ_r completely, then the time-dependent effective relative velocity can be further modified.

However, under the commonly employed tilted polishing mode (i.e., $n_1 \neq 0$ and $n_2 = 0$) [16,25], it becomes much simpler, because the effective relative velocity acting on this arbitrary point P in the contact area always keeps invariant with the changing of t, thus Eqs. (11) and (21) can be adopted directly. Consequently, the simulated results of effective relative velocities within the contact area of $a = 2.5$ mm could be plotted in Fig. 4. At first glance from Fig. 4(a), the 3D relative velocity distribution of $R_w = 60$ mm representing concave surface shows no significant discrepancy with that of $R_w \rightarrow \infty$ representing flat surface, but the slight difference still could be recognized from Fig. 4(b), in which y_P varies from -2.5 to 2.5 and $x_P = 0$, where the effective relative velocity of flat surface always greater than that of $R_w = 60$ mm, nonetheless, the two can be equal with each other just at the position of $x_P = 0$, $y_P = 0$. Further, more values of R_w are selected to study the influence of R_w on relative velocity, as observed from Fig. 4(c), the bigger the R_w, the larger the effective relative velocity, except for that at the position of $(x_P, y_P) = (0, 0)$. Additionally, by incorporating Fig. 4(a), Fig. 4(b) and Fig. 4(c), the effective relative velocity decreases with the growth of y_P when both x_P and R_w are determined. Indeed, these described phenomena can be visually interpreted by Fig. 4(d) via swing arm on the plane $O_A Y_A Z_A$, they are l_{c1}, l_{c2}, l_{c3} related to concave surface and l_{f1}, l_{f2}, l_{f3} associated with flat surface, respectively. The lengths among these swing arms can be compared and sorted as $l_{f1} > l_{c1} > l_{c2} = l_{f2} > l_{f3} > l_{c3}$, the longer the swing arm, the greater the linear velocity with the same n_1, which correspondingly explains the results seen in Fig. 4(b), as well as those in Fig. 4(a) and Fig. 4(c). Actually, the effective relative velocities acting on those points $(x_P, y_P) = (0, y_P)$ are a little special owing to that the velocity components V_{Py} in Eq. (11) and $^{B}V_{P\_Cy}$ in Eq. (21) both become zero, so that the visual interpretation can be conducted through Fig. 4(d). By the way, the effective relative velocity for flat surface deduced in Eq. (11) is confirmed to be correct, which agrees with the Ref. [36]. The relationship between effective relative velocities under different polishing modes has also been summarized in Fig. 5 vividly.

In Fig. 5, there are four cases of the effective relative velocity. Both CASE 1 and CASE 2 correspond to "periodic change with time", in which CASE 1 refers to the effective relative velocity for polishing curved surface under continuous precession mode, so the workpiece curvature effect cannot be neglected and $n_1 \neq 0$, $n_2 \neq 0$. Equation (21) includes the workpiece curvature radius as well as the nonzero n_1 and n_2, but the periodic time-dependent effect is not incorporated, thus Eq. (22) representing the periodic time-dependent effect should be considered together. Here, the derived Eq. (21) itself can be seen as the instantaneous relative velocity with regard to the nonzero n_2, while the relationship between n_2 and the polishing time t is available by Eq. (22). Afterwards, based on CASE 1, if the value of workpiece radius R_w is replaced by infinity, then CASE 2 can be easily obtained. When $n_1 \neq 0$ and $n_2 = 0$, it belongs to the tilted polishing mode, even though the time-dependent effect is taken into account, the effective relative velocity of arbitrary point P on the contact area always keeps invariable over time. Based on CASE 1, if the value of n_2 is set as zero, CASE 3 can be achieved. Similarly, based on CASE 3, if the value of workpiece radius R_w is replaced by infinity, then CASE 4 would be available.
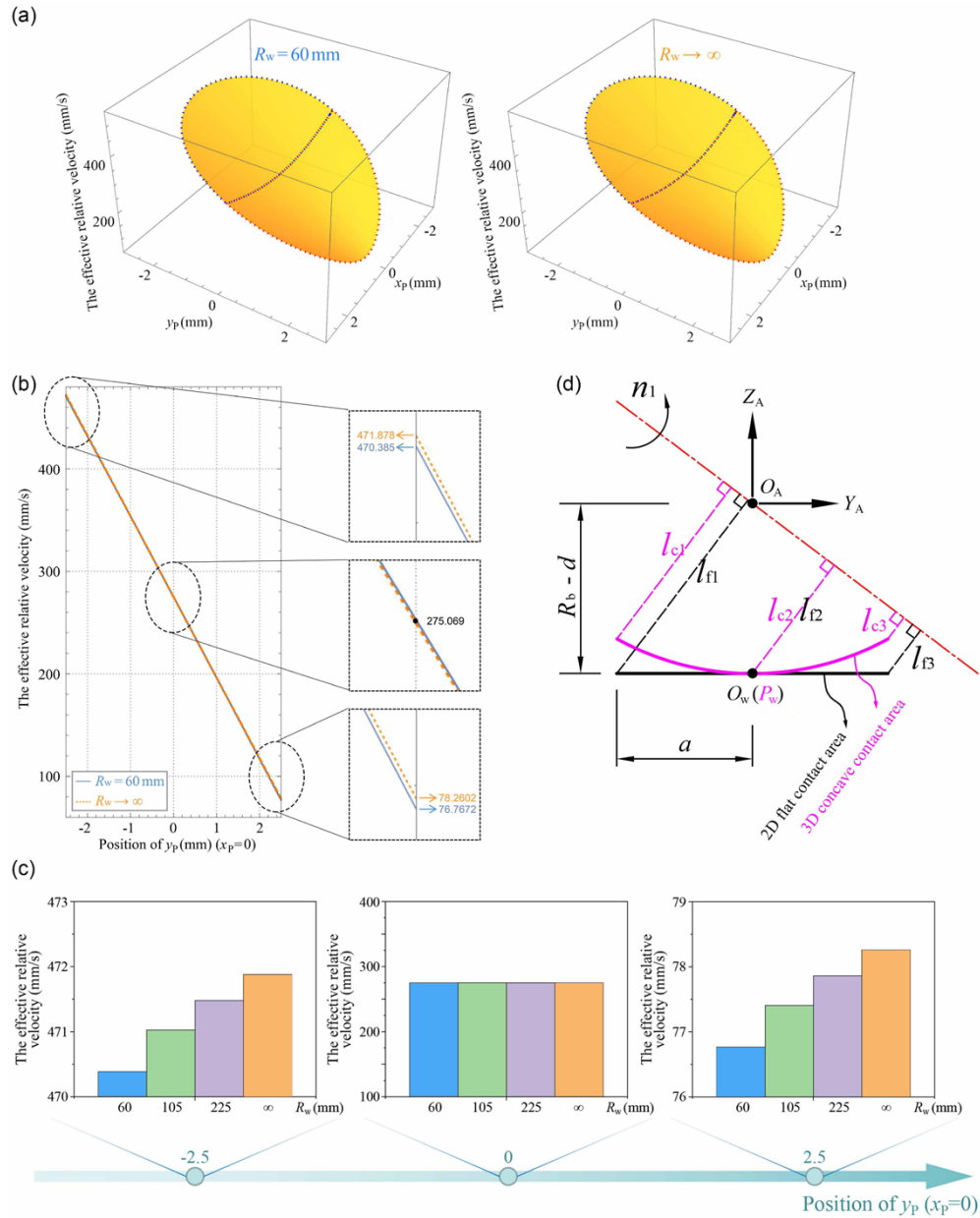
Fig. 4. Simulated results of effective relative velocities within the contact area of $a = 2.5$ mm (Given parameters: $R_b = 10$ mm, $d = 0.4$ mm, $\phi = 20$ deg, $n_1 = 800$ rpm, $n_2 = 0$ rpm) (a) comparison of 3D relative velocities between $R_w = 60$ mm and flat surface, (b) comparison of relative velocities between $R_w = 60$ mm and flat surface with the position of y_P from -2.5 to 2.5 and $x_P = 0$, (c) influence of R_w on relative velocity, and (d) interpretation to the difference between relative velocities via swing arm length.
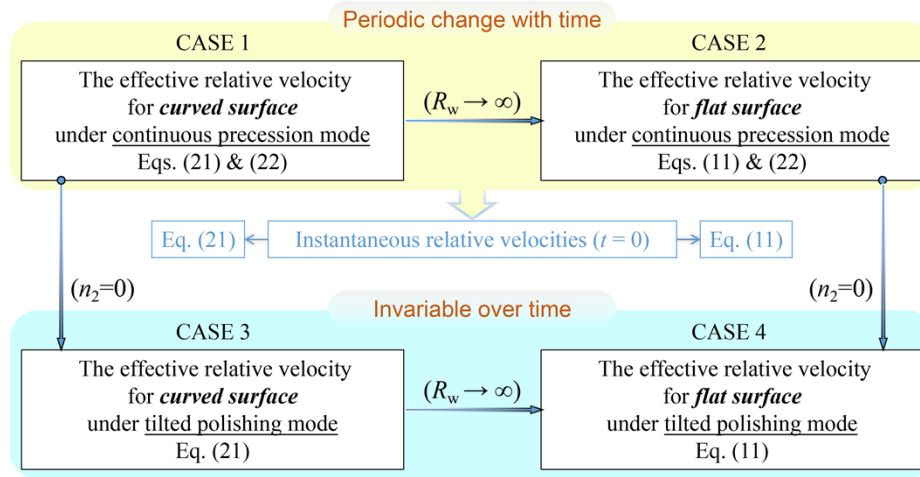
Fig. 5. Relationship between effective relative velocities under different polishing modes.

Hence, the most generic should be CASE 1, while CASE 4 becomes relatively special among the total four cases.

2.2. Determination of the contact pressure distribution

The pressure distribution in the contact area is usually thought to be complex, which can be attributed to multiple factors such as the polishing pad properties, the hydrodynamic force induced by slurry at the interface, the viscoelastic characteristics of ball-end tool, and so on [28]. If the curvature effect is put into consideration again, the situation must then be more complicated inevitably.

On the basis of elastic sphere-sphere contact mechanics, the determination of elastic pressure distribution on a curved workpiece [33,37] could be reasonably referenced, where one sphere is assumed to be largely rigid and the other is compliant. This pressure distribution is given as follows:

$$\sigma = \frac{F}{\pi \cdot a^2} \cdot \sqrt{1 - \frac{x_P^2 + y_P^2}{a^2}} \cdot e^{(x_P^2 + y_P^2)/2R_w \cdot h} \tag{23}$$

$$a = \frac{\sqrt{d(d - 2R_w)(d - 2R_b)(2R_w - d + 2R_b)}}{2R_w - 2d + 2R_b} \tag{24}$$

where h signifies a best fit constant, and F denotes the applied load which could be solved by [33]

$$F = \frac{3E_t}{4\kappa R_b}(2R_b d_{tc} - d_{tc}^2)^{3/2} \tag{25}$$

where E_t represents the effective tool modulus and κ is a constant. As a geometric parameter, by incorporating with Fig. 6, d_{tc} can be obtained through [19]

$$d_{tc} = d - \frac{d_h}{2}, \text{ for convex surface; } d_{tc} = d + \frac{d_h}{2}, \text{ for concave surface;}$$
$$d_h = \frac{2R_b d - d^2}{2(R_w - R_b + d)} \tag{26}$$

Based on Eq. (25) and Eq. (26), the qualitative relationship between F and R_w could be figured out, as shown in Fig. 7. For convex surface, the greater the R_w, the larger the F, nevertheless, for concave surface, with the growth of R_w, F decreases gradually. When $R_w \to \infty$, both concave
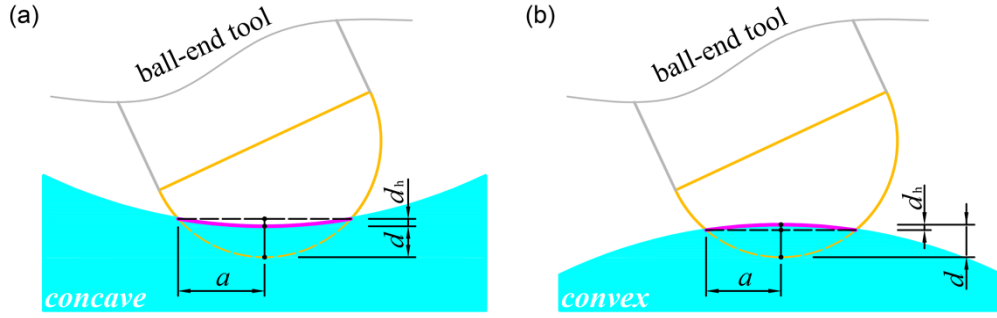
Fig. 6. Calculation of geometric parameter d_{tc} (a) for concave surface, and (b) for convex surface.

and convex surfaces tend to be flat surface so that the same F occurs. Moreover, due to the unknown E_t and κ, Eq. (25) can also be quantitatively written as

$$F(R_w) = \left(\frac{a_0 + b_0 R_w + c_0 R_w^2}{(d_0 + R_w)^2} \right)^{1.5} \tag{27}$$

where the four coefficients a_0, b_0, c_0, and d_0 can be determined by fitting the experiment data of F. As a result, Eq. (27) is supposed to be confirmed as an alternative method for calculating F in our research, as well as σ further.
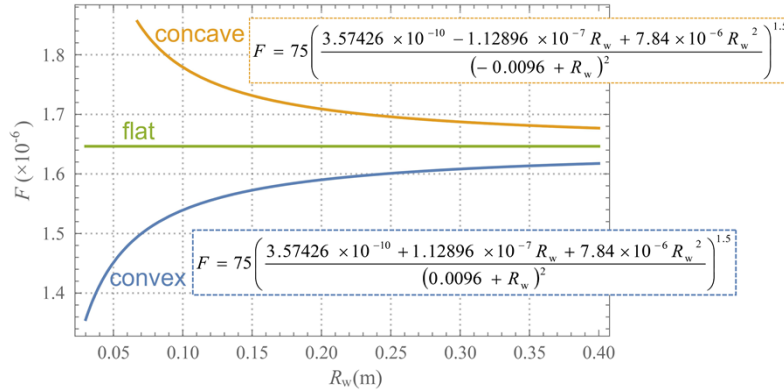
Fig. 7. Qualitative variation of F with the changing R_w (Given parameters: $R_b = 10$ mm, $d = 0.4$ mm, and suppose $E_t = \kappa = 1$).

2.3. Material removal model

According to Eq. (1), Eq. (21) and Eq. (23), the material removal depth at point P under tilted polishing mode is then determined by

$$MRD(x_P, y_P) = MRD(^A x_P, \, ^A y_P) = K\sigma Vt = K\sigma \cdot (^B V_{P\_C\_eff}) \cdot t \tag{28}$$

However, $K \cdot \sigma$ also has another mathematical form as follows:

$$K \cdot \sigma = K \cdot \frac{F}{\pi \cdot a^2} \cdot \sqrt{1 - \frac{x_P^2 + y_P^2}{a^2}} \cdot e^{(x_P^2 + y_P^2)/2R_w \cdot h} = K \cdot F \cdot \sigma_0 \tag{29}$$

Thus, Eq. (28) could be expressed as

$$MRD(x_P, \ y_P) = KF\sigma_0(h) \cdot ({}^{B}V_{P\_C\_eff}) \cdot t \tag{30}$$

where K usually is solved by experiment as [18,19,24,36]

$$K = \frac{MRD_{exp}}{F\sigma_0(h)^B V_{P\_C\_eff}t} \tag{31}$$

Here, Eq. (31) can be adjusted further as

$$K \cdot F = \frac{MRD_{exp}}{\sigma_0(h)^B V_{P\_C\_eff}t} \tag{32}$$

where MRD_{exp} denotes the actual experimental material removal depth at point P. Therefore, the experimental value of $K \cdot F$ corresponding to R_w can be available via Eq. (32). In order to obtain the fitting function of $K \cdot F$ with regard to R_w, the reasonable fitting relationship between them is needed to be determined. Owing to that K is considered as a constant, the mathematical format of F in Eq. (27) can be referenced to establish the fitting function of $K \cdot F$ with R_w. Substituting the achieved fitting function of $K \cdot F$ with R_w into Eq. (30), the material removal model can become concrete and clear. The flow chart of determining MRD model also has been drawn in Fig. 8.
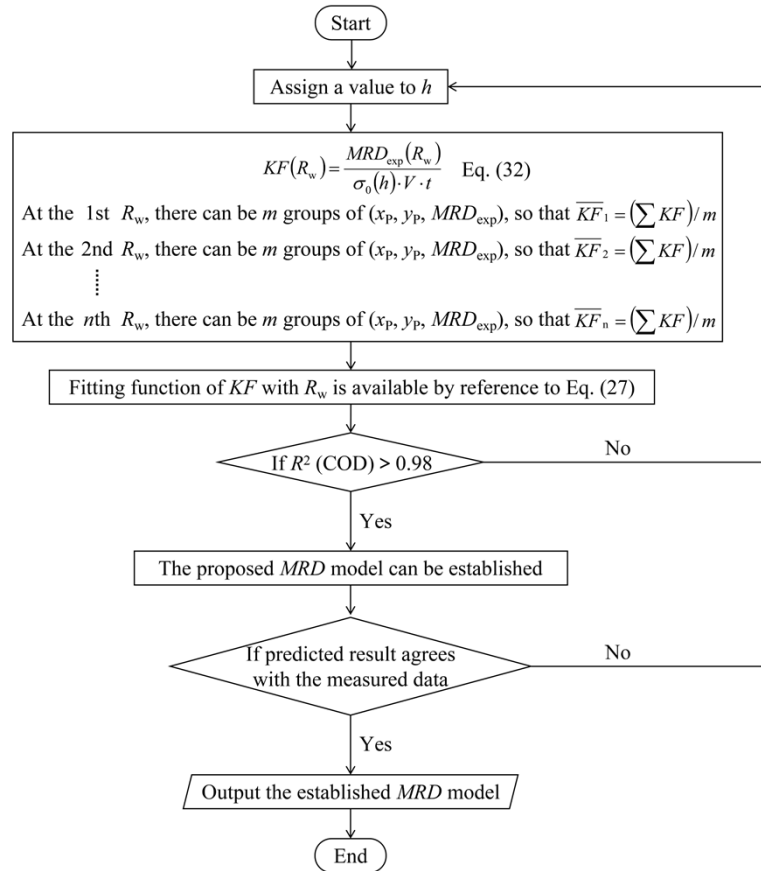
Fig. 8. Flow chart of determining *MRD* model.

As illustrated in Fig. 8, the initial value of h is essential to be assigned first, the selected range of h in our research is located between 30 μm [33] and 100 μm. Then, MRD_{exp} should be measured by several experimental polishing spots aiming to obtain the fitting function of $K \cdot F$ with R_w as referring to Eq. (32) and Eq. (27). If R^2 (COD)< 0.98, the value of h has to be adjusted based on the dichotomy method. And this is the first adjustment of h. Afterwards, the proposed MRD model can be specifically expressed by substituting the obtained fitting function of $K \cdot F$ with R_w into Eq. (30). Here, the comparison between the predicted result and the measured data must be conducted. If the predicted result cannot agree with the measured one, then the value of h needs to be adjusted again. Accordingly, Fig. 8 also indicates the determination of h.

3. Experimental

### 3.1. Design of the flexible ball-end tool

The flexible ball-end tool utilized in the polishing experiments is well designed and precisely fabricated, as exhibited in Fig. 9. This tool consists of three parts, from bottom to top, they are tool rod made of AL6061 aluminum alloy, natural rubber via injection molding, and polishing pad with the material of polyurethane, respectively. Where the Shore Hardness of natural rubber in Fig. 9(b) is 60 HA, and the edge of polishing pad shown in Fig. 9(c) is redundant and needs to be cut properly according to the design. The model number of adopted polishing pad is LP-57 (Universal Photonics Inc., USA) with density of 32 LB/FT^3 and Shore Hardness of 88 HA, as well as the thickness of 2 mm. There also have the through-hole and several annular grooves designed in the tool rod with the purpose of making the combination between rubber and tool rod become as firm and steady as possible. The other size parameters have been marked in Fig. 9(a).

The process of the polyurethane pad sticks to the ball-end tool can be illustrated by Fig. 9. As shown in Fig. 9(d), the first step is to obtain the polyurethane pad with the desired radius. The mechanical fixture is essential and prepared. The flat polyurethane pad should be put between the base and the end cover at the beginning, then tighten all the screws. Here, the radius of protrusion on the base is the same to that of the ball tool seen in Fig. 9(a), otherwise, the fabricated polyurethane pad is not fitted to the ball tool completely. Next, the whole mechanical fixture with the clamped polyurethane pad needs to be heated for 2~3 hours under the temperature of 140~160°C. After cooling, the deformed part of the polyurethane pad must be cut down carefully. The second step refers to pasting the cut polyurethane pad onto the ball-end polishing tool by utilizing the fast-setting epoxy adhesive or other effective binders evenly, and the standing time cannot be less than 8 hours. The third step is to cut away the redundant of the polyurethane pad, as shown in Fig. 9(c).

The aforementioned three steps are considered as the key preparation procedure to obtain the flexible ball-end polishing tool employed in our study. It was actually proven that the wrinkling could be avoided, and the spot polishing experiments were conducted successfully.

3.2. Experimental procedure

As shown in Fig. 10, the employed flexible ball-end polishing tool is assembled on the main spindle of Zeeko IRP 200 ultra-precision freeform polishing machine, a series of spot polishing experiments are conducted on those concave workpieces with the radii ranged from 75 mm to 225 mm. All of the workpieces are made of steel (S136) and fixed on C axis of Zeeko machine, and they are measured by Zygo Nexview 3D Optical Surface Profiler after the experiments. The concentration of adopted slurry is approximately 7 wt.% of Al_2O_3 abrasives with an average size of 3 μm, and the brand is FUJIMI. The process parameters are listed as follows: $R_b = 12$ mm, $d=$ 0.4 mm, $\phi = 20$ deg, $n_1 = 800$ rpm, $n_2 = 0$ rpm, which is the same as the simulated condition as shown in Fig. 4. The controlled polishing time is 120 s. In addition, the repeated experiments can be done via the rotation of C axis on Zeeko machine, there are three repeated polishing spots
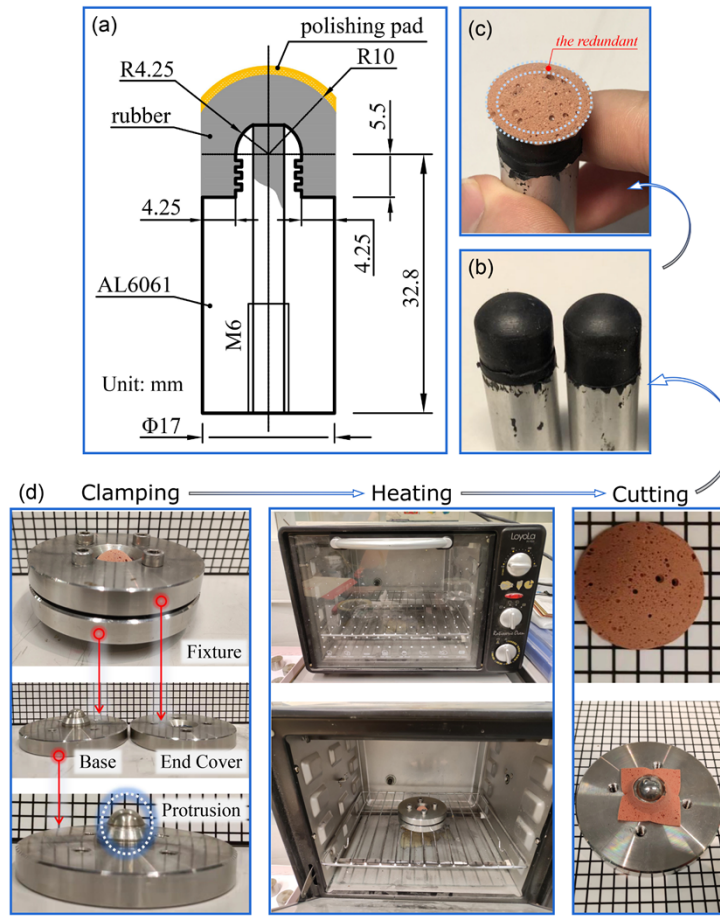
Fig. 9. The employed flexible ball-end polishing tool (a) design drawing, (b) injection molded with natural rubber, and (c) with polishing pad, and (d) fabricating process of polishing pad.

marked with 1, 2 and 3 in Fig. 10. The accomplishment of repeated experiments is illustrated in Fig. 11 in extraordinary detail. Here, Fig. 11(a) shows the vertical polishing that means the relative velocity of central point in the contact area is zero, and the path of these abrasive particles in the contact area also emerges to be concentric, which is not a disordered polishing track, so the vertical polishing is generally not selected and adopted. Figure 11(b) and (c) show the tilted polishing, but the latter can well repeat the spot polishing experiment on a workpiece for many times, it could be realized by rotating the C axis of Zeeko machine, on which the polished concave workpiece is fixed. In this study, the tilted polishing mode 2 in Fig. 11(c) is chosen to explore the material removal model with curvature effect, so the workpiece needs to be adjusted by an angle ϕ_0 during the corresponding measurement in order to observe the polished spots clearly. According to the developed tool influence function model, the whole 3D topography of the polishing spot can be affected by the tool radius R_b. There has no specific definition to the tool size for polishing flat surface, whereas the tool radius must be chosen properly for polishing those curved workpieces. As long as the flexible ball-end tool and the curved workpiece do not interfere with each other, the corresponding tool radius can be reasonably adopted.

**Fig. 10.** Spot polishing experiment conducted on Zeeko IRP200 machine.
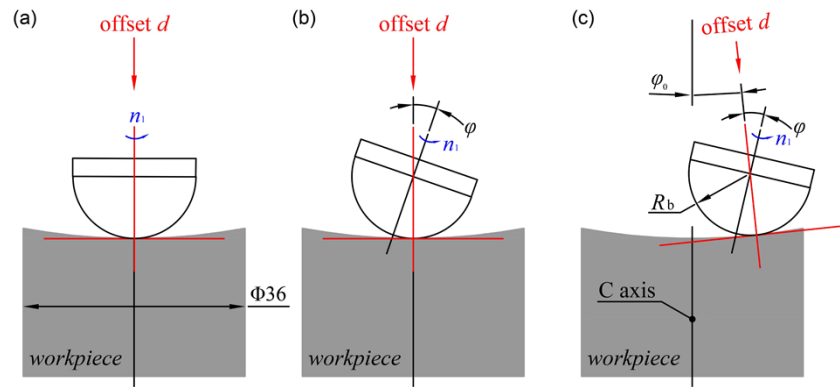
Fig. 11. Three contact states between the flexible ball-end polishing tool and the concave surface (a) vertical polishing, (b) tilted polishing 1, and (c) tilted polishing 2.

3.3. Results

Before presenting the comparison between predicted results and measured data, on the basis of Fig. 8, the term of $K \cdot F$ involved in *MRD* model shown in Eq. (30) must be identified experimentally in advance. In order to reduce the computation burden, the values of m and n are set as 2 and 4, respectively. To be specific, $K \cdot F$ could be determined through $(x_P, y_P, MRD_{exp}) = (0, 0, MRD_{exp1})$ and $(0, a/2, MRD_{exp2})$ at one certain R_w so that the corresponding average value of $K \cdot F$ can be unequivocal, while the four R_w are adopted as 75 mm, 95 mm, 105 mm and 225 mm orderly. According to the dichotomy method, 82 μm of h becomes acceptable and applied ultimately after iteration. Figure 12 shows the fitting function of $K \cdot F$ with R_w and its R^2 of 0.99 also is extremely close to 1, in which the mathematical expression and variation curve of $K \cdot F$ demonstrates similarity to Eq. (27) as well as the curve drawn in Fig. 7, respectively.

Indeed, $K \cdot F$ and F exhibit the similar change trend with variation of R_w due to the invariable Preston coefficient K during the polishing process. Furthermore, the order of magnitude of K cannot be ignored casually, some common values of K are available and they could be 10^{-14} [19], 10^{-8} [24], 10^{-13} [36] and so on. Then, the order of magnitude difference between $K \cdot F$ and F cannot be neglected, and it will be reflected on those four fitting coefficients a_0, b_0, c_0, and d_0.
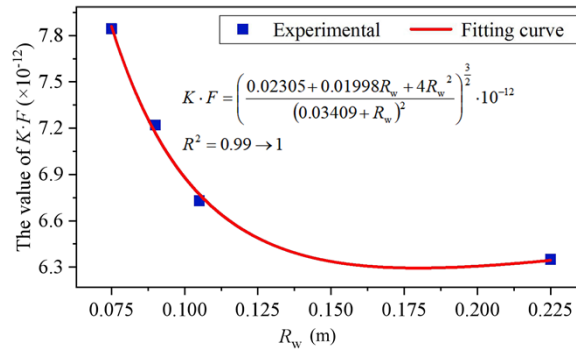
**Fig. 12.** Fitting function of $K \cdot F$ with changing of R_w.

As a result, Eq. (30) should be specifically written as

$$MRD(x_P, y_P) = (-1)\left(\left(\frac{0.02305 + 0.01998R_w + 4R_w{}^2}{(0.03409 + R_w)^2}\right)^{\frac{3}{2}} \times 10^{-12}\right) \cdot \sigma_0(h = 82 \times 10^{-6}) \cdot {}^B V_{P\_C\_eff} \cdot t$$

(33)

where the unit of MRD is meter, and the extra added term (-1) represents the material removal depth below the initial unpolished surface aiming to compare with the experimental profile of polishing spot clearly.

Figure 13 gives the comparison between experimental and predicted polishing spots, in which both 2D and 3D topographies are available, and the workpiece of concave surface with $R_w = 90$ mm is taken as the illustrated case study. Figure 13(a2), Fig. 13(b2) and Fig. 13(c2) show the experimentally measured data, so do Fig. 13(a3), Fig. 13(b3) and Fig. 13(c3). Despite the former three are the same to the latter three correspondingly, different colors are utilized just to help to strengthen the understanding of experimental phenomena. Furthermore, the curvature effect indicated in Fig. 13(c2) and Fig. 13(c3) must be eliminated during the measurement. Otherwise, the experimental polishing spot cannot be extracted and compared with the predicted result effectively. There also are many scratches found to be existed on the surface of polishing spot, which is caused by the action of abrasive particles in the slurry during polishing. Besides, the actual rotation of flexible ball-end tool should be explained by referring to Fig. 13(b2) and Fig. 13(b3) with the markers of IN and OUT. As observed in Fig. 13(a1) and Fig. 13(b1), the theoretically calculated 2D and 3D topographies can be obtained. The predicted polishing spot is ideal and symmetric about the central axis (i.e., $(x_P = 0, y_P)$), thus, there have Region L and Region R, and it also is seen as a standard circle via top view, as found in Fig. 13(a1). Moreover, the deduced maximum removal depth is figured out to be located in the area of $y_P < 0$ according to Fig. 13(b1). Three axes of x_P, y_P and z_P shown in Fig. 13 all correspond to those plotted in Fig. 1 and Fig. 2 precisely. It is also observed that the shape of measured polishing spot is a bit like an ellipse that emerges symmetry about the central axis, too. Additionally, the maximum removal depth also occurs in the area of $y_P < 0$, which coincides with the prediction. However, the significant discrepancy between theoretical prediction and measured data could be captured, and it refers to the nonuniform material removal. More specifically, the actual amount of material removal in Region L is greater than that in Region R, whereas the material removal in Region R1 is also much larger than that acted in Region R2.

Furthermore, targeted at providing comprehensive insights into material removal mechanism during polishing by the designed flexible ball-end polishing tool shown in Fig. 9, the section profiles of experimental and predicted polishing spots along the central axis with a wide range of R_w from 75 mm to 225 mm are also presented comparatively, as shown in Fig. 14 clearly. It can
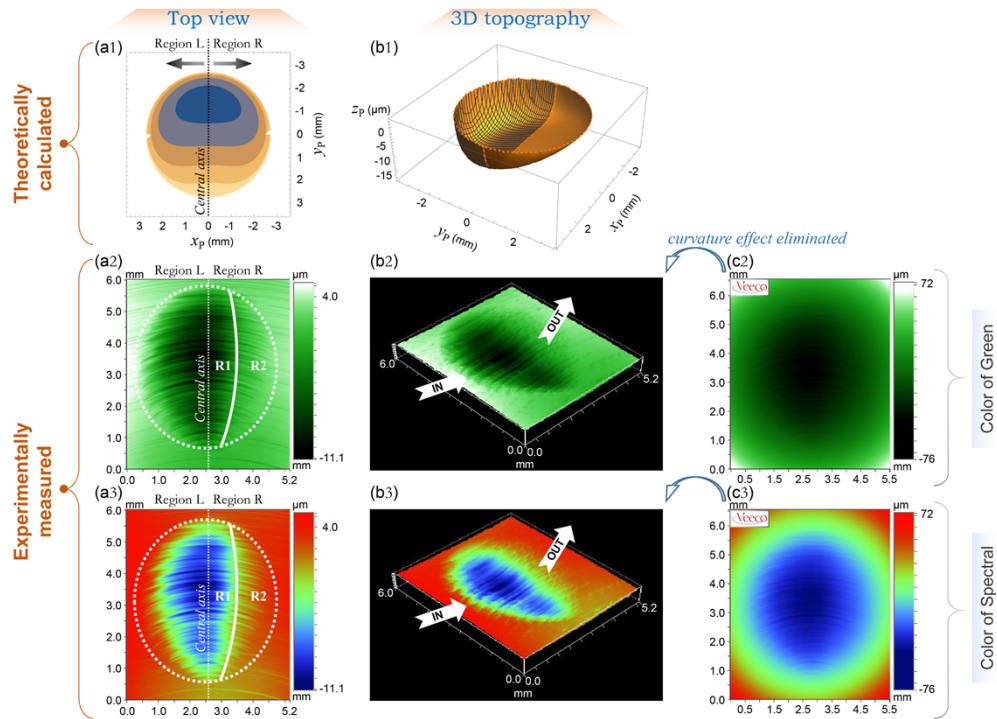
Fig. 13. Comparison between experimental and predicted polishing spots for the case of $R_w = 90$ mm (a1) top view of theoretically calculated polishing spot, (b1) 3D topography of theoretically calculated polishing spot, (a2)&(a3) top view of experimentally measured polishing spot, (b2)&(b3) 3D topography of experimentally measured polishing spot, (c2)&(c3) 2D topography of experimentally measured polishing spot with curvature effect.

be quantitatively noticed that the predictions match well with the experiments, and the maximum material removal depth decreases with the gradual growth of R_w. Indeed, the maximum removal depth is located in the area of $y_P < 0$, which agrees well with the results shown in Fig. 13. In addition, the length size of measured polishing spot along the central axis can also be predicted reasonably. It is also noted that the theoretically calculated section profile exhibits idealization and smoothness, nevertheless, the measured section profile displays high frequency fluctuation, which could be attributed to the interaction between abrasive particles in slurry and the polished surface, as well as the experimental environment in the actual polishing process. On the whole, the effectiveness and correctness of the proposed *MRD* model can be validated reasonably through a serious of spot polishing experiments.

The formation of elliptical spot during actual polishing process may be attributed to the contact pressure induced by the relative velocity [17], which is also influenced by the material property of the flexible rubber tool. This phenomenon is also found in some previous published papers [19,28,36]. The rotational direction of the flexible ball-end tool is parallel to the short axis of elliptical polishing area, as shown in Fig. 13, the direction of "IN"-"OUT" matches with the short axis of elliptical polishing spot. As a comparison, the length of long axis of elliptical polishing area that shown in Fig. 14 can still be predicted well, and there is no significant velocity effect along the long axis of elliptical polishing area.

There also have an initial curve in Fig. 14 and it is a straight line. This initial straight line refers to the original surface contour of unpolished concave workpiece that the curvature effect has been eliminated during the measurement, as shown in Fig. 13(b2) and (b3), so the experimental
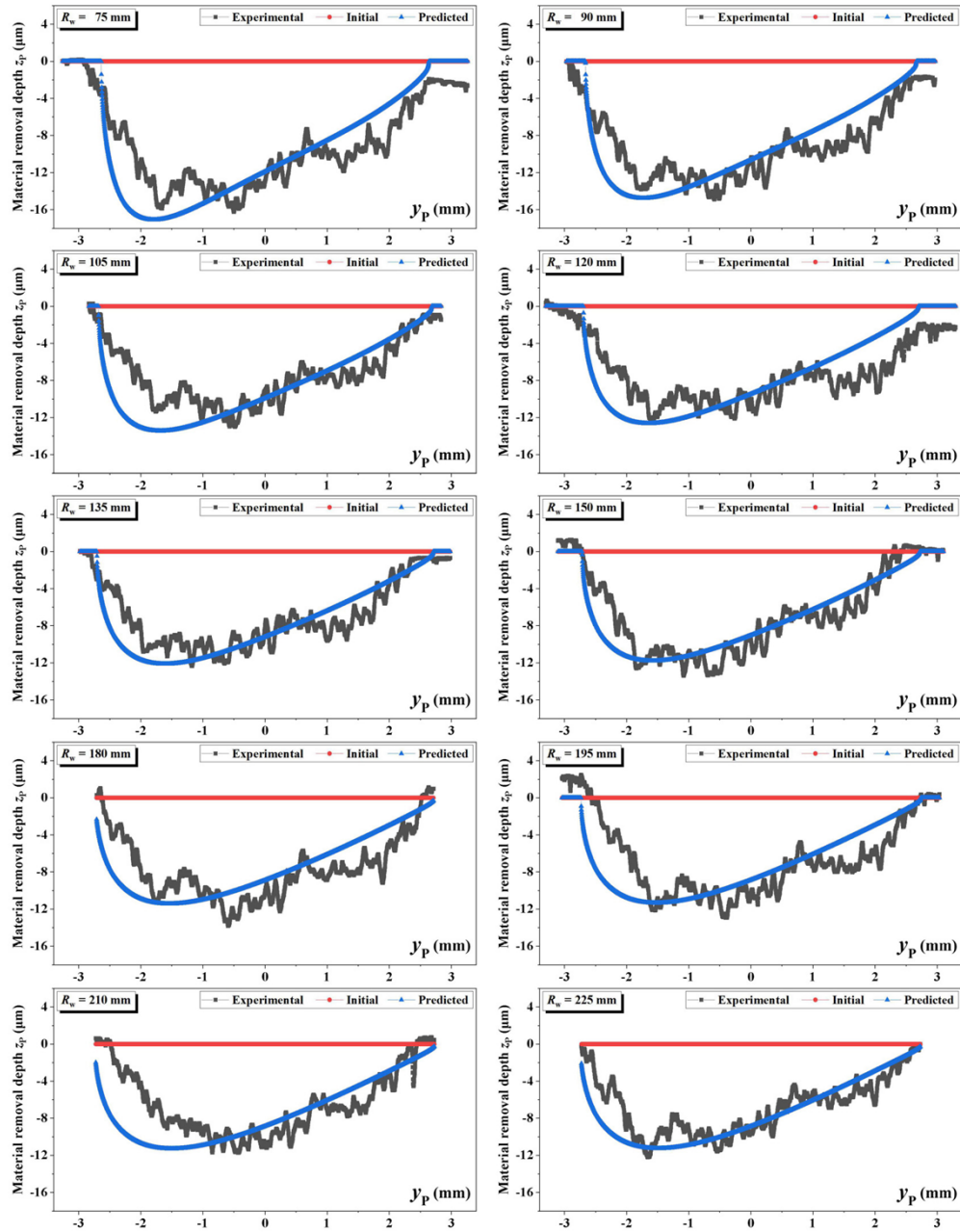
Fig. 14. Section profiles of experimental and predicted polishing spots along the central axis (i.e., $(x_P = 0, y_P)$).

polishing spot can be extracted and compared with the predicted result effectively and clearly. If the experimental polishing spot is directly measured without eliminating curvature of the workpiece, the measured result is the same to that presented in Fig. 13(c2) and Fig. 13(c3), and the experimental polishing spot cannot be observed well, which could be interpreted by the scale difference between the experimental polishing spot and the surface contour of workpiece. The former is in micrometer (μm) level, while the latter is in millimeter (mm) level. As a result, the comparative analysis in Fig. 14 is undertaken on the basis of the eliminated curvature effect during the measurement.

In addition, there are several sub-graphs in Fig. 14 that do not perfectly exhibit the complete consistency between the predicted curve and the experimental curve, especially at $y_P < 0$. However, it is still considered to be acceptable and credible because the trend of the prediction matches with the experimental results on the whole range of y_P from -3 mm to +3 mm among the total ten sub-graphs. Also, some regularities have already been predicted clearly. For example, the maximum removal depth, which is one of the important evaluation indicators [17,29], decreases with increasing R_w when R_w is less than 225 mm. Although the degree of consistency between the predicted data and the experimental result is expected to be as high as 100%, but this is not possible owing to the uncertainty during the actual polishing process, such as the fluctuation of the slurry concentration, wear of the polishing pad, etc. Hence, it is still convincing since those significant regularities could been presented properly.

4. Discussion

The experimental results of nonuniform material removal can be divided mainly into two aspects. Along the direction of y_P axis as shown in Fig. 14, the maximum removal depth is not located in the midpoint but appears in the area of $y_P < 0$, which should be interpreted by the coupling effect of effective relative velocity together with contact pressure according to the theoretical modeling described in Section 2. However, the contact pressure distribution is about rotational symmetry of z_P axis, as plotted in Fig. 15. So let look back to the effective relative velocity distribution as indicated in Fig. 4(a), it does exhibit non-uniform distribution and much higher velocity can be obtained in the area of $y_P < 0$ rather than that of $y_P > 0$. Accordingly, the sectional profile of the polishing spot can be conjectured qualitatively and drawn schematically via Fig. 16. When $y_P > 0$, it is easy to understand that, the trend of the variation of the removal profile is monotonically decreasing owing to that both effective relative velocity and contact pressure present monotonic decreasing characteristics. When $y_P < 0$, one is monotonically decreasing but the other monotonically rises, which then causes the appearance of maximum removal depth. Moreover, it can be quantitatively assessed that, the maximum removal depth does decrease with the increase of R_w suggested in Fig. 14. The changing of R_w can lead to the variations of both contact pressure and effective relative velocity. Nevertheless, the contact pressure decreases but the effective relative velocity increases with the gradual growth of R_w, as shown in Fig. 15(b) and Fig. 4, respectively. As a result, the contact pressure can be confirmed to play a more significant role in material removal comparing to the effective relative velocity.

On the other hand, the nonuniform material removal refers to the Region L and Region R observed in Fig. 13. Due to the multidisciplinary and multi-scale complexity during actual polishing process, it could be attributed to several probable reasons as discussed as follows. The first explanation should be associated with the dynamic contact pressure for a rolling sphere [16,38], which shows slight difference from the ideal static contact pressure as observed in Fig. 15. As shown in Fig. 17, the actual contact pressure consists of the elastic stress σ^{el} together with the dissipative stress σ^{dis}, when it is Region L corresponding to "IN" marked in Fig. 13(b2) and Fig. 13(b3), the total pressure is a sum of σ^{el} and σ^{dis}, whereas Region R corresponds to "OUT" and the total pressure becomes $\sigma^{el} - \sigma^{dis}$. The greater the actual contact pressure, the larger the material removal. As a result, the actual amount of material removal in Region L
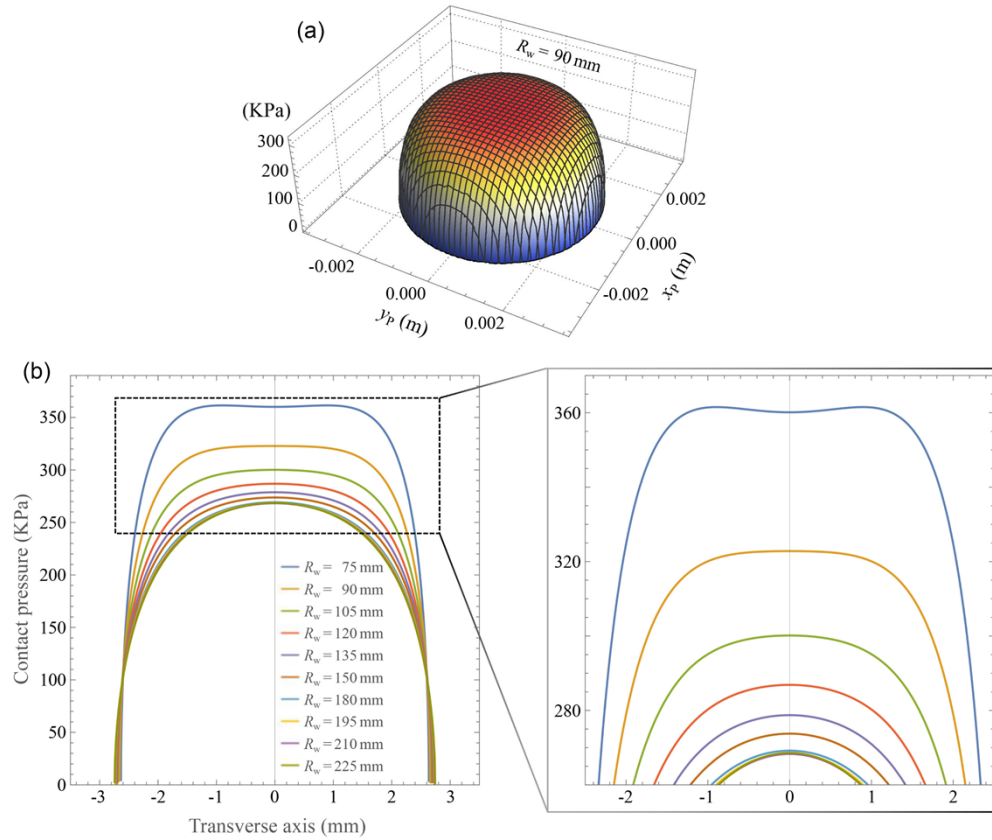
Fig. 15. Contact pressure distribution (a) the three dimensional distribution for case of $R_w = 90$ mm, and (b) section profiles ranged from $R_w = 75$ to 225 mm.
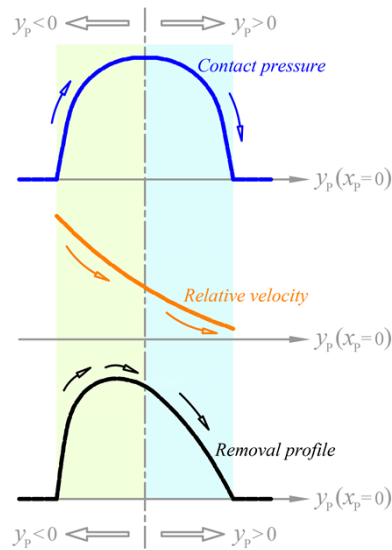

Fig. 16. Qualitative analysis on the section profile of polishing spot.

can be greater than that in Region R. Hence, during the actual experiment, the contact pressure distribution between the workpiece and ball-end tool is asymmetrical. The second factor is supposed to be linked to the discontinuity of slurry during polishing. Inspired by the research work [16], the contact pressure in/around the position of $(x_P, y_P) = (0, 0)$ is considerably high that has been indicated in Fig. 15 and Fig. 17, so that the slurry film may be broken up, which prevents abrasive particles in the slurry from acting on Region R effectively. In other words, the combined action of both the abrasive wear induced by abrasive particles in the slurry and the wear effect from polishing pad asperities does result in the material removal of workpiece surface [17,29]. Consequently, the numerous lack of abrasive particles acting on Region R is properly inferred as another cause for the nonuniform material removal between Region L and Region R, as depicted in Fig. 17. Furthermore, the third interpretation is relevant to the interfacial fluid pressure that produces sub-ambient and positive pressures at the leading edge ("IN" similarly shown in Fig. 13) and the trailing edge ("OUT" analogously seen from Fig. 13), respectively [39]. The former tends to "pull" the polishing pad and the workpiece surface into intimate contact, as well as improves the slurry flow into the interface. In contrast, the latter tends to "squeeze out" the slurry from the trailing edge ("OUT"), which may cause a "driving force" that resists the backward flowing of slurry and retards the slurry replenishment [39]. Accordingly, it can be understood likely as that the active abrasive particles working on Region L are more than those on Region R, which is not contradictory with the second illustration mentioned above.
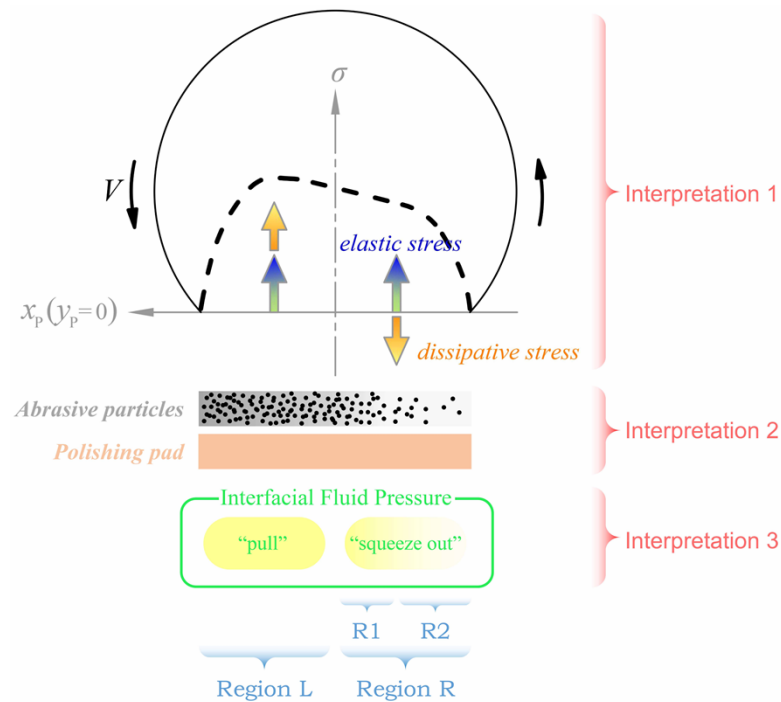
Fig. 17. Interpretations for the nonuniform material removal between Region L and Region R.

Despite the workpiece curvature effect was also taken into consideration in the previous research work conducted by [19,33], it is only $R_w = 500\,\text{mm}$ and $R_w \rightarrow \infty$ (i.e., flat surface) that were investigated for concave surface. In addition, when the curvature radius was transferred from $R_w = 500\,\text{mm}$ to $R_w \rightarrow \infty$, different change trends of maximum removal depths were experimentally presented between their investigations, and it was slight positive correlation in

(a)

(b)

(c)
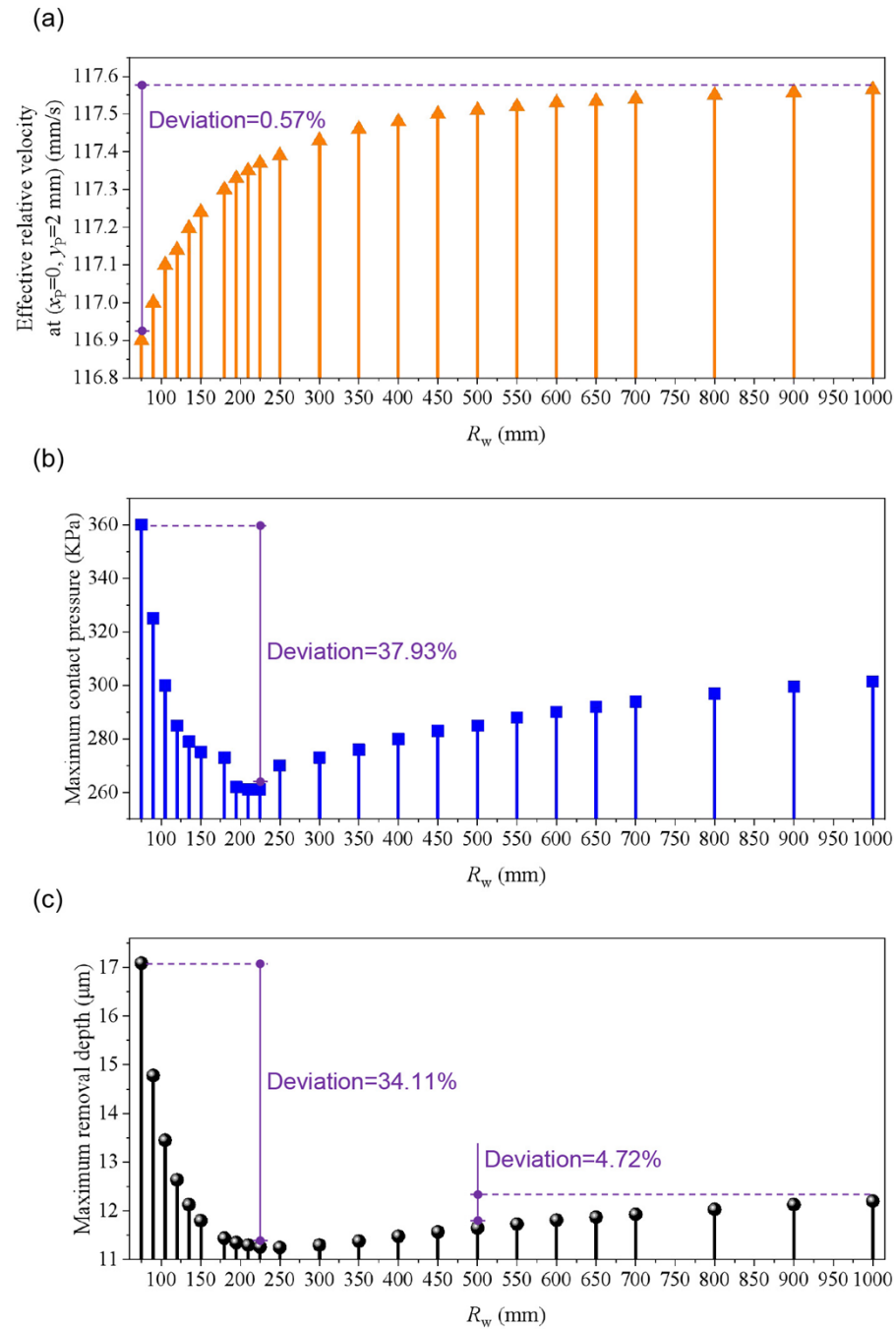
Fig. 18. Curvature effect within a broad range (a) effective relative velocity (taking the point (x_P=0, y_P= 2 mm) as the case), (b) maximum contact pressure, and (c) maximum removal depth.

[19] but negative correlation given oppositely in [33], which might have been attributed to different styles and sizes of polishing tools, various process parameters, as well as the discrepancy of actual polishing environment, etc. Here, aiming to figure out the variation trend of maximum removal depth within a much broader range of R_w in detailed, besides those shown in Fig. 14, R_w from 250 mm to 1000 mm also are added and studied successively, then the corresponding maximum removal depths can be calculated on the basis of the developed *MRD* model conveniently, as drawn in Fig. 18.

It is interesting to note in Fig. 18(c) that $R_w = 225$ mm can be captured as an inflection point. The maximum removal depth declines sharply with increasing R_w when R_w is less than 225 mm, whereas it gradually increases with increasing R_w when R_w exceeds 225 mm. The occurrence of the inflection point of R_w can be analyzed by the performances of two sub-models involved in the developed material removal model. One is the effective relative velocity and the other refers to the contact pressure. Compared with the effective relative velocity, the contact pressure should be confirmed to play a more significant role in material removal incorporated with curvature effect, since the change trend of contact pressure shown in Fig. 18(b) correspondingly exhibits similarity to the variation trend of the maximum removal depth observed from Fig. 18(c), whereas the effective relative velocity shown in Fig. 18(a) keeps growing with the rising of R_w in the whole range from 75 mm to 1000 mm, as well as the extremely small deviation of 0.57%. What is more, the limited growth rate of 4.72% of maximum removal depth starting from $R_w = 500$ mm to $R_w \rightarrow \infty$ also is illustrated in Fig. 18(c), which becomes helpful to understand the slight difference between those two researches [19,33], and this insignificant difference may result from the reasonable errors such as the error in measurement, the error in calculation and so on.

5. Conclusions

Ultra-precision polishing of optical surfaces can be regarded as a complex process. Targeted at figuring out the influence of changing curvature on material removal and revealing the in-depth understanding of material removal mechanisms, systematic investigation on the workpiece curvature effect is conducted both theoretically and experimentally in polishing with a flexible ball-end tool in this paper. The study can serve as a foundation for polishing freeform workpiece with deterministic removal and is also expected to be valuable to peer researchers. The major findings have been summarized as follows.

(1) Inspired by the macro-scale Preston equation, the material removal model incorporating curvature effect is successfully determined by two sub-models. One is the generic model of effective relative velocity based on kinematic theory, and the other is a semi-experimental contact pressure model on the basis of elastic sphere-sphere contact mechanics. Hence, the 3D surface topographies of polishing spots can be simulated. A series of spot polishing experiments have been conducted on concave surfaces with a broad curvature radius ranging from 75 mm to 225 mm. The predicted sectional profiles of the polishing spots agree reasonably well with the experimental results, which verifies the effectiveness of the proposed material removal model.

(2) Two nonuniform material removal phenomena are found experimentally under tilted polishing mode. Along the central axis marked on polishing spot, the maximum removal depth is not located in the midpoint but appears on the side of $y_P < 0$, which results from the coupling effect of effective relative velocity with nonuniform distribution and contact pressure with rotational symmetry. Besides, the material removal at Region L and that at Region R are not symmetrical about the central axis, and much greater removal amount occurs at Region L, which may be attributed to nonuniform applied working pressure, discontinuous slurry flow, and interfacial fluid pressure effect, etc.

(3) According to the theoretical contrastive analyses of effective relative velocities between the concave surface and the flat surface, it is found that the effective relative velocity increases slightly with gradual increase of the curvature radius, except for that of the center point on contact area, due to different swing arm lengths. Furthermore, with the increase of curvature radius from 75 mm to 1000 mm, the effective relative velocity shows a limited increase trend with a total deviation of 0.57%, whereas the changing trend of maximum contact pressure corresponds to that of maximum removal depth very well, so the contact pressure should be confirmed to play a more significant role in material removal.

Symbols

MRD	material removal depth	K	Preston coefficient
σ	applied working pressure	V	relative velocity
t	certain polishing time (dwell time)	R_b	radius of the used flexible ball-end tool
d	offset	a	radius of the circular contact area
R_w	workpiece curvature radius	ω_1	angular velocity of L axis
ϕ	inclination angle	ω_2	angular velocity of Z_A axis
α	angle between $O_w Z_A$ axis and $O_A P$ axis	θ	angle between $O_w P$ and $O_w N$
n_1	tool rotational speed of L axis	n_2	tool rotational speed of Z_A axis
F	applied load	h	a best fit constant
E_t	effective tool modulus	κ	a constant
V_{P1}	relative velocity induced by L axis	V_{P2}	relative velocity induced by Z_A axis
V_P	relative velocity induced by L and Z_A axes		
V_{P_eff}	projection of vector V_P into the plane $X_A O_A Y_A$		
P_{ij}	any point located on the three dimensional contact area		
P_w	point on the bottom of three dimensional contact area		
P_{ij}'	projection of P_{ij} into the plane 1		
d_0	perpendicular gap between P_w and the plane 1		
β	angle between tangent plane ij and horizontal plane $X_A O_A Y_A$		
$^A V_{P1\_C}$	relative velocity by L axis considering curvature effect		
$^A V_{P2\_C}$	relative velocity by Z_A axis considering curvature effect		
$^A V_{P\_C}$	relative velocity induced by L and Z_A axes considering curvature effect		
$^B V_{P\_C}$	rotation transformation from $^A V_{P\_C}$		
$^B V_{P\_C\_eff}$	projection of vector $^B V_{P\_C}$ into the plane $X_b O_b Y_b$		
$\{A\}$	space rectangular coordinate system fixed on the ball-end tool		
$\{B\}$	attained by the rotation of $\{A\}$ around $O_A Z_A$ axis with an angle of θ		
$\{w1\}$	space rectangular coordinate system fixed at center of the concave workpiece		
$\{w2\}$	achieved via the rotation of $\{w1\}$ around $O_{w1} Z_{w1}$ axis with an angle of θ		
θ_r	relative position of arbitrary point P to the ball-end tool		
a_0, b_0, c_0, d_0	four fitting coefficients on the fitting function of $K \cdot F$ (or F) with R_w		
$(^A x_P, {}^A y_P, {}^A z_P)$	the coordinates of point P_{ij}		
l_{c1}, l_{c2}, l_{c3}	swing arm related to concave surface		
l_{f1}, l_{f2}, l_{f3}	swing arm associated with flat surface		
d_{tc}, d_h	geometric parameter for determination of the contact pressure distribution		

References

1. H. Y. Lyu, L. B. Kong, S. X. Wang, and M. Xu, "Robust and accurate measurement of optical freeform surfaces with wavefront deformation correction," Opt. Express **30**(5), 7831–7844 (2022).
2. S. S. Chen, S.M. Yang, Z. R. Liao, C. F. Cheung, Z. D. Jiang, and F. H. Zhang, "Curvature effect on surface topography and uniform scallop height control in normal grinding of optical curved surface considering wheel vibration," Opt. Express **29**(6), 8041–8063 (2021).
3. T. Suratwala, J. Menapace, R. Steele, L. Wong, G. Tham, N. Ray, B. Bauman, M. Gregory, and T. Hordin, "Mechanisms influencing and prediction of tool influence function spots during hemispherical sub-aperture tool polishing on fused silica," Appl. Opt. **60**(1), 201–214 (2021).
4. L. J. Ren, G. P. Zhang, L. Zhang, Z. Zhang, and Y. M. Huang, "Modelling and investigation of material removal profile for computer controlled ultra-precision polishing," Precis. Eng. **55**, 144–153 (2019).
5. L. Zhang, H. Y. Tam, C. M. Yuan, Y. P. Chen, and Z. D. Zhou, "An investigation of material removal in polishing with fixed abrasives," Proc. Inst. Mech. Eng., Part B **216**(1), 103–112 (2002).
6. Z. B. Xia, F. Z. Fang, E. Ahearne, and M. R. Tao, "Advances in polishing of optical freeform surfaces: A review," J. Mater. Process. Technol. **286**, 116828 (2020).
7. W. L. Liao, Y. F. Dai, X. H. Xie, and L. Zhou, "Microscopic morphology evolution during ion beam smoothing of Zerodur® surfaces," Opt. Express **22**(1), 377–386 (2014).
8. A. Beaucamp, Y. Namba, and R. Freeman, "Dynamic multiphase modeling and optimization of fluid jet polishing process," CIRP Ann. **61**(1), 315–318 (2012).
9. C. J. Wang, C. F. Cheung, L. T. Ho, M. Y. Liu, and W. B. Lee, "A novel multi-jet polishing process and tool for high-efficiency polishing," Int J Mach Tool Manu. **115**, 60–73 (2017).
10. M. Y. Chen, Y. T. Feng, Y. J. Wan, Y. Li, and B. Fan, "Neural network based surface shape modeling of stressed lap optical polishing," Appl. Opt. **49**(8), 1350–1354 (2010).
11. T. Wang, H. B. Cheng, Y. Chen, and H. Tam, "Multiplex path for magnetorheological jet polishing with vertical impinging," Appl. Opt. **53**(10), 2012–2019 (2014).
12. A. Beaucamp and Y. Namba, "Super-smooth finishing of diamond turned hard X-ray molding dies by combined fluid jet and bonnet polishing," CIRP Ann. **62**(1), 315–318 (2013).
13. A. Beaucamp, Y. Namba, and P. Charlton, "Corrective finishing of extreme ultraviolet photomask blanks by precessed bonnet polisher," Appl. Opt. **53**(14), 3075–3080 (2014).
14. D. Walker, G. Y. Yu, H. Li, W. Messelink, R. Evans, and A. Beaucamp, "Edges in CNC polishing: from mirror-segments towards semiconductors, paper 1: edges on processing the global surface," Opt. Express **20**(18), 19787–19798 (2012).
15. D. D. Walker, D. Brooks, A. King, R. Freeman, R. Morton, G. McCavana, and S. W. Kim, "The 'Precessions' tooling for polishing and figuring flat, spherical and aspheric surfaces," Opt. Express **11**(8), 958–964 (2003).
16. Z. C. Cao and C. F. Cheung, "Multi-scale modeling and simulation of material removal characteristics in computer-controlled bonnet polishing," Int. J. Mech. Sci. **106**, 147–156 (2016).
17. C. Shi, Y. F. Peng, L. Hou, Z. Z. Wang, and Y. B. Guo, "Micro-analysis model for material removal mechanisms of bonnet polishing," Appl. Opt. **57**(11), 2861–2872 (2018).
18. W. L. Zhu and A. Beaucamp, "Investigation of critical material removal transitions in compliant machining of brittle ceramics," Mater. Des. **185**, 108258 (2020).
19. B. Zhong, C. J. Wang, X. H. Chen, and J. Wang, "Time-varying tool influence function model of bonnet polishing for aspheric surfaces," Appl. Opt. **58**(4), 1101–1109 (2019).
20. X. L. Ke, C. J. Wang, Y. B. Guo, and Q. Xu, "Modeling of tool influence function for high-efficiency polishing," Int J Adv Manuf Tech. **84**(9), 2479–2489 (2016).
21. F. W. Preston, "The theory and design of plate glass polishing machines," Journal of Glass Technology. **11**(44), 214–256 (1927).
22. S. Y. Zeng and L. Blunt, "Experimental investigation and analytical modelling of the effects of process parameters on material removal rate for bonnet polishing of cobalt chrome alloy," Precis. Eng. **38**(2), 348–355 (2014).
23. C. Wang, Z. Wang, Q. Wang, X. Ke, B. Zhong, Y. Guo, and Q. Xu, "Improved semirigid bonnet tool for high-efficiency polishing on large aspheric optics," Int J Adv Manuf Tech. **88**(5-8), 1607 (2017).
24. C. F. Cheung, L. B. Kong, L. T. Ho, and S. To, "Modelling and simulation of structure surface generation using computer controlled ultra-precision polishing," Precis. Eng. **35**(4), 574–590 (2011).
25. R. Pan, B. Zhong, D. J. Chen, Z. Z. Wang, J. W. Fan, C. Y. Zhang, and S. N. Wei, "Modification of tool influence function of bonnet polishing based on interfacial friction coefficient," Int J Mach Tool Manu. **124**, 43–52 (2018).
26. G. Shi and B. Zhao, "Modeling of chemical-mechanical polishing with soft pads," Appl. Phys. A: Mater. Sci. Process. **67**(2), 249–252 (1998).

27. Zhang, A. A. Busnaina, J. Feng, and M. A. Fury, "Particle adhesion force in CMP and subsequent cleaning processes," *Proc. Fourth Int. Chemical-Mechanical Planarization for ULSI Multilevel Interconnection Conf.* 1999: 61–64.

28. Z. C. Cao, C. F. Cheung, and X. Zhao, "A theoretical and experimental investigation of material removal characteristics and surface generation in bonnet polishing," Wear. **360-361**, 137–146 (2016).

29. C. C. Shi, Y. F. Peng, L. Hou, Z. Z. Wang, and Y. B. Guo, "Improved analysis model for material removal mechanisms of bonnet polishing incorporating the pad wear effect," Appl. Opt. **57**(25), 7172–7186 (2018).

30. J. F. Song and Y. X. Yao, "Material removal model considering influence of curvature radius in bonnet polishing convex surface," Chin. J. Mech. Eng. (Engl. Ed.) **28**(6), 1109–1116 (2015).

31. J. F. Song, Y. X. Yao, D. G. Xie, B. Gao, and Z. J. Yuan, "Effects of polishing parameters on material removal for curved optical glasses in bonnet polishing," Chin. J. Mech. Eng. (Engl. Ed.) **21**(05), 29–33 (2008).

32. J. F. Song, Y. X. Yao, Y. G. Dong, and B. Dong, "Prediction of surface quality considering the influence of the curvature radius for polishing of a free-form surface based on local shapes," Int J Adv Manuf Tech. **95**(1-4), 11–25 (2018).

33. T. Suratwala, J. Menapace, G. Tham, R. Steele, L. Wong, N. Ray, B. Bauman, M. Gregory, and T. Hordin, "Effect of workpiece curvature on the tool influence function during hemispherical sub-aperture tool glass polishing," Appl. Opt. **60**(4), 1041–1050 (2021).

34. M. Y. Yang and H. C. Lee, "Local material removal mechanism considering curvature effect in the polishing process of the small aspherical lens die," J. Mater. Process. Technol. **116**(2-3), 298–304 (2001).

35. C. C. Shi, Y. F. Peng, L. Hou, Z. Z. Wang, Y. B. Guo, Q. L. Tang, C. L. Li, and D. L. Chen, "Investigation on the nonlinear relationship between relative velocity and material removal in bonnet polishing," *The 9th International Symposium on Advanced Optical Manufacturing and Testing Technologies: Subdiffraction-limited Plasmonic Lithography and Innovative Manufacturing Technology. International Society for Optics and Photonics*, 2019, 10842: 108420K.

36. C. Wang, Z. Wang, X. Yang, Z. Sun, Y. Peng, Y. Guo, and Q. Xu, "Modeling of the static tool influence function of bonnet polishing based on FEA," Int J Adv Manuf Tech. **74**(1-4), 341–349 (2014).

37. A. C. Fischer-Cripps, "The Hertzian contact surface," J. Mater. Sci. **34**(1), 129–137 (1999).

38. N. V. Brilliantov and T. Pöschel, "Rolling friction of a viscous sphere on a hard plane," EPL (Europhysics Letters) **42**(5), 511–516 (1998).

39. C. H. Zhou, L. Shan, J. R. Hight, S. H. Ng, and S. Danyluk, "Fluid pressure and its effects on chemical mechanical polishing," Wear **253**(3-4), 430–437 (2002).